J*f***M** PAPERS

Roughness-induced boundary-layer instability beneath internal solitary waves

Andres Posada-Bedoya[1] , Jason Olsthoorn[1] and Leon Boegman[1]

[1]Department of Civil Engineering, Queen's University, Kingston, ON K7L 3N6, Canada
Corresponding author: Andres Posada-Bedoya, 21afpb@queensu.ca

We investigate the effects of bottom roughness on bottom boundary-layer (BBL) instability beneath internal solitary waves (ISWs) of depression. Applying both two-dimensional (2-D) numerical simulations and linear stability theory, an extensive parametric study explores the effect of the Reynolds number, pressure gradient, roughness (periodic bump) height h_b and roughness wavelength λ_b on BBL instability. The simulations show that small h_b, comparable to that of laboratory-flume materials (~ 100 times less than the thickness of the viscous sublayer δ_v), can destabilize the BBL and trigger vortex shedding at critical Reynolds numbers much lower than what occurs for numerically smooth surfaces. We identify two mechanisms of vortex shedding, depending on h_b/δ_v. For $h_b/\delta_v \gtrsim 1$, vortices are forced directly by local flow separation in the lee of each bump. Conversely, for $h_b/\delta_v \lesssim 10^{-1}$ the roughness seeds perturbations in the BBL, which are amplified by the BBL flow. Roughness wavelengths close to those associated with the most unstable BBL mode, as predicted by linear instability theory, are preferentially amplified. This resonant amplification nature of the BBL flow, beneath ISWs, is consistent with what occurs in a BBL driven by surface solitary waves and by periodic monochromatic waves. Using the N-factor method for Tollmien–Schlichting waves, we propose an analogy between the roughness height and seed noise required to trigger instability. Including surface roughness, or more generally an appropriate level of seed noise, reconciles the discrepancies between the vortex-shedding threshold observed in the laboratory versus that predicted by otherwise smooth-bottomed 2-D spectral simulations.

Key words: boundary layer stability, solitary waves, topographic effects

A. Posada-Bedoya, J. Olsthoorn and L. Boegman

1. Introduction

Internal solitary waves (ISWs) are nonlinear waves of large amplitude that can propagate tens to hundreds of kilometres along the pycnoclines of lakes and coastal oceans. As they shoal, ISWs of depression interact with the bottom boundary-layer (BBL) (Trowbridge & Lentz 2018) by imposing a streamwise velocity (pressure) distribution that is maximum (minimum) under the trough. The ISW-imposed pressure leads to rapid, unsteady acceleration and deceleration of the BBL flow beneath the front and rear shoulders of the ISW, respectively (e.g. Boegman & Stastna 2019; Zulberti *et al.* 2020). For large-amplitude ISWs propagating over a flat bottom, laboratory experiments (Carr *et al.* 2008; Aghsaee & Boegman 2015; Zahedi *et al.* 2021) and numerical simulations (Diamessis & Redekopp 2006; Aghsaee *et al.* 2012; Sakai *et al.* 2020; Ellevold & Grue 2023; Posada-Bedoya *et al.* 2024) have demonstrated that ISW-induced currents can lead to hydrodynamic instabilities in the BBL. At laboratory scales ($Re_{ISW} \sim \mathcal{O}(100)$, defined in § 1.2), the instability is convective (Posada-Bedoya *et al.* 2024), as it falls behind the ISW. The instabilities in the BBL may be amplified by the flow (Huerre & Monkewitz 1990; Schmid & Henningson 2001), depending on the magnitude and energy distribution of the background seed noise (Verschaeve & Pedersen 2014; Posada-Bedoya *et al.* 2024) as well as the characteristics of the BBL flow (Reynolds number and pressure gradient) (Aghsaee *et al.* 2012).

Parameterizing and understanding the mechanisms leading to BBL instability beneath ISWs is crucial for closing ISW energy budgets (Moum *et al.* 2007*b*; Zahedi *et al.* 2021) and predicting sediment transport processes (Boegman & Stastna 2019). Internal solitary waves carry significant energy shoreward (Chang *et al.* 2006; Shroyer *et al.* 2010), and as they approach the continental shelf, their energy is dissipated largely as a result of strong bottom interaction (Boegman *et al.* 2005; Moum *et al.* 2007*a*; Aghsaee *et al.* 2010). Therefore, the stability of the BBL beneath ISWs will determine dissipation (Klymak & Moum 2003; Shroyer *et al.* 2009) and propagation distances (Shroyer *et al.* 2010; Zahedi *et al.* 2021, 2023): unstable waves have dissipative length scales of ~100 wavelengths, whereas stable waves propagate significantly further, ~1000 wavelengths. Predicting the BBL stability is also important for closing the turbulent kinetic energy budget in the BBL. Enhanced near-bed shear, induced by the passage of ISWs, has been shown to increase both production and dissipation rate in the BBL by three orders of magnitude (Zulberti *et al.* 2020, 2022). This, in turn, has direct implications for the sediment resuspension and transport (Stastna & Lamb 2008; Boegman & Stastna 2019).

Part of the difficulty in understanding the transition from laminar to turbulent flow lies in the number of factors that affect the transition, the most important ones being the pressure distribution in the external flow, the wall roughness and the characteristics of disturbances in the free-stream flow (Schlichting 1968). Previous studies on ISW-induced BBL instability have focused on the distribution of the external flow, by varying the pressure gradient and Reynolds number imposed by the ISW on the BBL (e.g. Diamessis & Redekopp 2006; Aghsaee *et al.* 2012; Ellevold & Grue 2023; Posada-Bedoya *et al.* 2024). In comparison, research on the roles of bottom roughness (e.g. Stastna & Lamb 2008; Carr *et al.* 2010) and of free-stream disturbances (e.g. Posada-Bedoya *et al.* 2024), in the ISW-induced BBL, remains scarce. Here, we focus on the role of bottom roughness in BBL instability beneath ISWs of depression.

1.1. *Roughness-induced BBL instability*

Simulations and laboratory experiments on the interaction of ISWs with rough bottom topography have considered topography with scales significantly larger than the induced

boundary-layer thickness (Stastna & Lamb 2008; Carr *et al.* 2010; Olsthoorn & Stastna 2014; Harnanan *et al.* 2015,2017). For example, Stastna & Lamb (2008) simulated the propagation of ISWs of elevation over topography modelled as the superposition of three sinusoids with a maximum roughness height (h_b) relative to the total depth H, $h_b/H = 0.03$. Carr *et al.* (2010) conducted two-dimensional (2-D) simulations and laboratory experiments of ISWs propagating over sinusoidal corrugated beds. They report the smallest topography in the literature beneath ISWs of depression, with $h_b/H \approx 10^{-2}$. In comparison, typical laboratory-flume bed materials for experiments on ISW-induced BBL instability including acrylic sediments (Aghsaee & Boegman 2015), smooth concrete (Zahedi *et al.* 2021) or glass (Carr *et al.* 2008), are expected to have relative roughness heights $h_b/H \sim 10^{-3}-10^{-6}$. Based upon our simulations, these can be 10–100 times smaller than the laminar viscous sublayer thickness (δ_v) of the ISW-induced BBL. Despite the known presence of surface roughness in laboratory flumes, and its known theoretical relevance for BBL stability (Schlichting 1968), the physical mechanisms underlying such small-scale roughness-induced transition beneath ISWs remain unknown.

The roughness-induced BBL instability beneath ISWs investigated here is similar to the related problem of roughness-induced BBL instability beneath surface solitary waves (SSWs) (Sumer *et al.* 2010; Scandura 2013) and surface periodic waves (Blondeaux & Vittori 1994). Wall roughness has been shown to introduce perturbations to the surface-wave-driven BBL that are preferentially amplified at the wavelength of the most unstable mode of the BBL, as predicted by linear stability theory (Blondeaux & Vittori 1994; Scandura 2013). The similarity of the BBL flow beneath SSWs and ISWs raises the question of whether the BBL exhibits the same resonator behaviour beneath ISWs. Both types of waves (SSWs and ISWs) impose an unsteady, isolated pair of favourable and adverse pressure gradients on the BBL, with an inflection point in the velocity profile upstream of the BBL separation (Sumer *et al.* 2010; Aghsaee & Boegman 2015). Also, for both types of waves, Verschaeve & Pedersen (2014) predicted noise-amplifier behaviour of the BBL, with the stability determined by the accumulated amplification of perturbations of small initial amplitude (potentially introduced by small-scale bottom roughness). However, for both types of BBL flow, different studies reported different critical Reynolds numbers associated with instability. This is potentially explained by differences in the background noise level (Verschaeve & Pedersen 2014).

1.2. *Vortex-shedding thresholds beneath ISWs*

Using 2-D spectral simulations, Aghsaee *et al.* (2012) argued that BBL instability under an ISW of depression was determined by the non-dimensional pressure gradient (P_{ISW}) and the momentum thickness Reynolds number (Re_{ISW}) at the separation point beneath the wave (figure 1), where

$$P_{ISW} = (U_2 + c)\frac{U_2}{L_w g'}, \tag{1.1}$$

$$Re_{ISW} = U_2\sqrt{\frac{L_w}{\nu (U_2 + c)}}. \tag{1.2}$$

Here, U_2 is the absolute value of the maximum horizontal velocity at the wave trough, c is the solitary wave phase speed, $g' = g\Delta\rho/\rho_0$ is the reduced gravity, g is the gravitational constant, $\rho_0 = 1000 \text{ kg m}^{-3}$ is a reference density, $\Delta\rho$ is the density difference across the pycnocline, ν is the kinematic viscosity and L_w is the horizontal wavelength
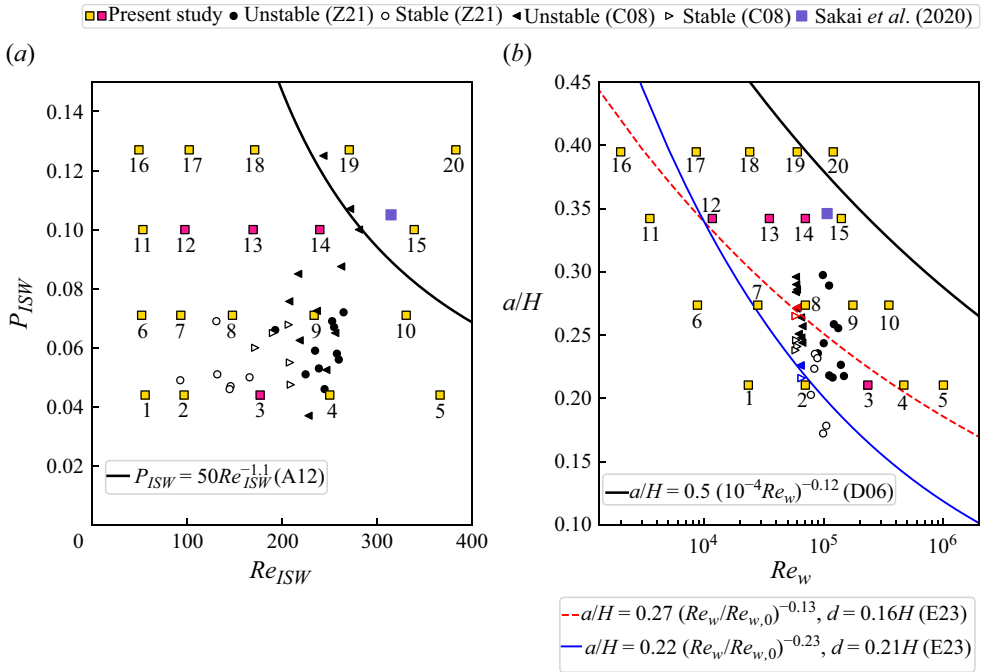
Figure 1. Stability diagrams in (*a*) Re_{ISW} versus P_{ISW} space and (*b*) a/H versus Re_w space, showing our simulated ISW cases (numbered yellow and pink squares), the laboratory observations by Zahedi *et al.* (2021) (Z21) (circles) and Carr *et al.* (2008) (C08) (triangles) and the unstable ISW numerically simulated by Sakai *et al.* (2020) (S20) (blue square). Pink squares highlight the selected ISW cases to focus on the description of the results. The ISW numeration corresponds with the one in table 1. Black solid lines are stability curves from spectral 2-D simulations by (*a*) Aghsaee *et al.* (2012) (A12) and (*b*) Diamessis & Redekopp (2006) (D06). Blue and red lines are stability curves from 2-D simulations by Ellevold & Grue (2023) (E23) for two different pycnocline depths (*d/H*). Blue and red markers are the associated laboratory experiments in Carr *et al.* (2008) selected by Ellevold & Grue (2023) to fit each stability curve. The C08, Z21 and E23 ISWs were generated by lock release, whereas the D06, A12, S20 and present study ISWs were generated by the solution of the Korteweg-de Vries (KdV) or DJL equations.

scale (Michallet & Ivey 1999)

$$L_w = \frac{1}{a} \int_{-\infty}^{\infty} \eta_p(x)\mathrm{d}x, \tag{1.3}$$

where $\eta_p(x)$ is the vertical displacement of the pycnocline and *a* is the wave amplitude. More recently, Ellevold & Grue (2023) conducted 2-D simulations to reproduce the laboratory experiments by Carr *et al.* (2008). They proposed that, in addition to a/H and $Re_w = c_0 H/\nu$, the pycnocline depth (*d*) is a relevant parameter for BBL stability. They defined a critical threshold of the form $a/H = a_0(Re_w/Re_{w0})^{-m_1}$, where the parameters a_0 and m_1 depend on the relative depth of the pycnocline (*d/H*). Here, c_0 is the linear wave phase speed.

At laboratory scales ($Re_{ISW} \sim \mathcal{O}(100)$), there is a discrepancy in the criteria for vortex shedding between experiments and spectral 2-D simulations (Aghsaee *et al.* 2012; Zahedi *et al.* 2021; Posada-Bedoya *et al.* 2024). Lock-release-generated ISWs generated in the laboratory (Carr & Davies 2006; Carr *et al.* 2008; Zahedi *et al.* 2021) and simulated by finite-volume 2-D solvers (Ellevold & Grue 2023) agree on the instability threshold, $Re_{ISW} \approx 200$ (figure 1*a*). However, 2-D spectral simulations of Dubreil–Jacotin–Long

(DJL)-initialized ISWs (Aghsaee *et al.* 2012; Posada-Bedoya *et al.* 2024) predict a critical threshold at higher (Re_{ISW}, P_{ISW}) (figure 1*a*). It remains unknown why the 2-D spectral simulations have a different stability threshold from that observed in the laboratory.

The convective noise-amplifier nature of the BBL (Verschaeve & Pedersen 2014; Posada-Bedoya *et al.* 2024) supports the hypothesis that wall roughness might provide a mechanism for introducing seed perturbations to the BBL, which are convectively amplified beneath the ISW. Roughness occurs naturally in the laboratory but is not explicitly considered in idealized smooth-bed numerical simulations (e.g. Aghsaee *et al.* 2012; Sakai *et al.* 2020; Posada-Bedoya *et al.* 2024). Therefore, roughness, as a source of perturbations, is a potential feature that might explain the discrepancies between the experimental and spectral 2-D numerical results. To this point, Verschaeve & Pedersen (2014) explain why Sumer *et al.* (2010), Vittori & Blondeaux (2011) and Ozdemir *et al.* (2013) each obtained different critical Reynolds numbers for the instability of the BBL beneath SSWs due to differences in background noise across their numerical and experimental conditions. A similar explanation, with roughness as the distinguishing feature of differences in background noise, can be argued for the ISW case. Related to the present study, Scandura (2013) simulated SSW propagation over random bottom roughness with average height $h_b \approx 5 \times 10^{-5}$ m to reproduce the laboratory observations by Sumer *et al.* (2010).

1.3. *Objectives*

The objective of the present study is to investigate how bottom roughness may seed BBL instability beneath ISWs of depression, at scales comparable to the roughness of typical materials encountered in laboratory flumes. Using 2-D simulations and linear stability theory, we conducted an extensive parametric study on the effects of resolved sinusoidal roughness parameters (height and wavelength) on BBL instability beneath ISWs. We described the destabilization mechanisms and computed instability thresholds for different roughness heights. By interpreting BBL–roughness interaction as a mechanism for seeding perturbations within the BBL, we predicted the background noise levels associated with the different roughness heights. Finally, we discussed the relevance of our results for more realistic random roughness heights.

2. Methods

2.1. *Problem definition*

We conducted 2-D simulations of ISWs propagating over a flat bottom and a region of sinusoidal roughness. The geometry of the sinusoidal roughness was determined by two parameters: height h_b and wavelength λ_b (figure 2*b*). The computational domain had a maximum depth H and a length $L = 16H$. The ISWs were initialized by numerically solving the DJL equation using the algorithm of Turkington *et al.* (1991) as implemented by Dunphy *et al.* (2011). The initial condition was given by the DJL solution with the ISW trough at $x = 0.25L$. As in Carr *et al.* (2010), the present domain comprised a section of flat bottom, followed by rough topography, to allow for illustration of the effects of roughness on BBL instability. The region of sinusoidal roughness was located at a distance of $3L_w$ from the initial ISW trough, sufficient for the BBL beneath the initially inviscid DJL wave to develop, before interacting with the roughness region. We verified that the results were insensitive to further increasing this distance (not shown). The length of the roughness region was $0.31L$, defined to accommodate 10 wavelengths of the largest
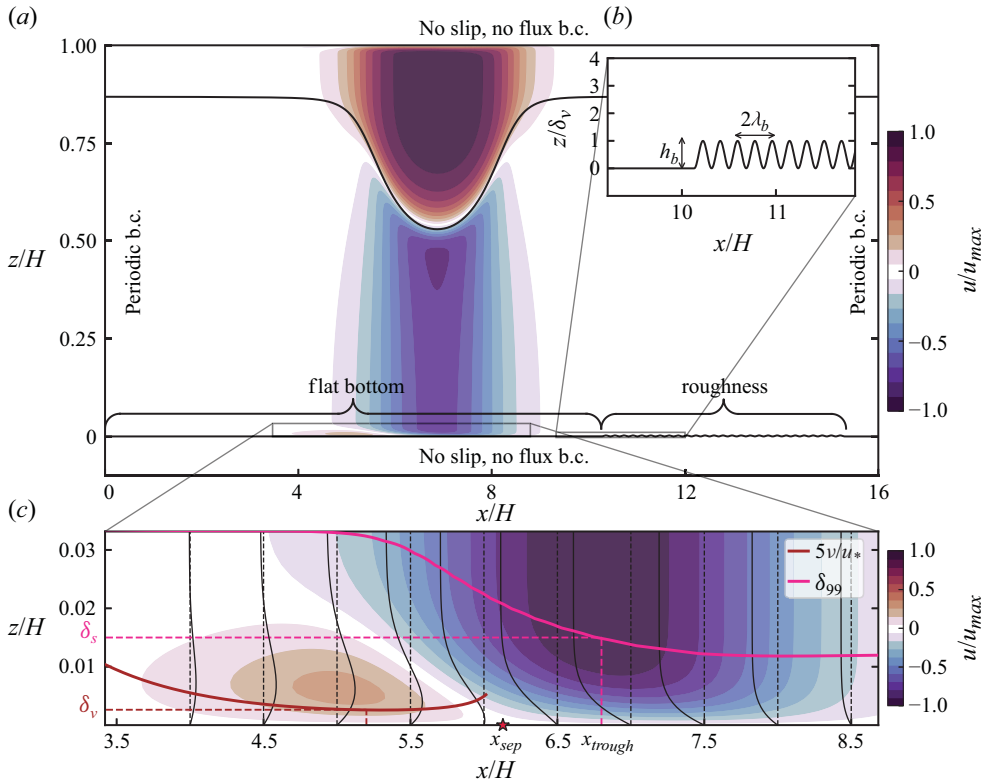
Figure 2. (*a*) Sketch of the domain, boundary conditions (b.c.), and the non-dimensional horizontal velocity field for the set-up of the numerical simulations. (*b*) Inset zoom of the bottom roughness elements indicates the roughness parameters (λ_b, h_b). (*c*) Inset zoom of the near-bed velocity indicates separation point (x_{sep}), and boundary-layer parameters δ_v and δ_s. As $u_* = 0$ at x_{sep}, values of $5\nu/u_*$ are only shown upstream of x_{sep}. Black lines show selected velocity profiles every $0.5x/H$, with the zero of each profile indicated with a vertical dashed line. Profiles were scaled to fit the $0.5x/H$ spacing.

simulated λ_b (table 1) while balancing the computational demand with the total domain length. The results were insensitive to further increasing the length of the roughness region (not shown). A schematic of the problem is presented in figure 2(*a, b*).

The roughness region was initiated and terminated with a minimum value of the sinusoidal function that defined the topography (see figure 2*b*). This created a smooth transition between the roughness region and the flat bottom. Therefore, even though the bottom slope is a continuous function, the second-order derivative of the topography is discontinuous at the flat–rough bottom transition. Hence, the flow at the edges of the roughness region was different from the flow over the periodic bumps. As we are focused on the BBL interaction with the periodic topography, the flow near the flat–rough transitions was not considered here in detail.

The ISWs propagated along a quasi-two-layer density stratification defined via a hyperbolic tangent profile, widely used in numerical studies

$$\bar{\rho}(z) = \rho_0 + \Delta\rho \tanh\left(\frac{z - z_{pyc}}{h_{pyc}}\right), \qquad (2.1)$$

ISW	z_{pyc}/H	L_w/H	P_{ISW}	a/H	Re_{ISW}	Re_w	δ_s/h_{b_0}	δ_v/h_{b_0}	λ_b^{OS}/L_w
1	0.15	1.61	0.044	0.21	56	2.34E+04	9.93	2.30	0.0836
2	0.15	1.61	0.044	0.21	97	7.01E+04	5.73	1.00	0.0459
3	0.15	1.61	0.044	0.21	177	2.34E+05	3.17	0.41	0.0246
3A[†]	0.15	1.61	0.044	0.21	177	2.34E+05	3.17	0.41	0.0082
3B[†]	0.15	1.61	0.044	0.21	177	2.34E+05	3.17	0.41	0.0738
4	0.15	1.61	0.044	0.21	250	4.68E+05	2.28	0.24	0.0180
5	0.15	1.61	0.044	0.21	367	1.00E+06	1.57	0.14	0.0131
6	0.15	1.81	0.071	0.27	52	8.77E+03	16.06	3.73	0.1076
7	0.15	1.81	0.071	0.27	94	2.81E+04	8.68	1.53	0.0640
8	0.15	1.81	0.071	0.27	148	7.01E+04	5.55	0.76	0.0407
8A[†]	0.15	1.81	0.071	0.27	148	7.01E+04	5.55	0.76	0.0136
8B[†]	0.15	1.81	0.071	0.27	148	7.01E+04	5.55	0.76	0.1221
9	0.15	1.81	0.071	0.27	234	1.75E+05	3.53	0.38	0.0262
10	0.15	1.81	0.071	0.27	331	3.51E+05	2.49	0.23	0.0203
11	0.13	2.35	0.100	0.34	54	3.51E+03	27.02	6.00	0.1689
12	0.13	2.35	0.100	0.34	98	1.17E+04	14.36	2.27	0.0906
13	0.13	2.35	0.100	0.34	170	3.51E+04	8.05	0.97	0.0570
13A[†]	0.13	2.35	0.100	0.34	170	3.51E+04	8.05	0.97	0.0190
13B[†]	0.13	2.35	0.100	0.34	170	3.51E+04	8.05	0.97	0.1711
14	0.13	2.35	0.100	0.34	240	7.01E+04	5.70	0.58	0.0425
15	0.13	2.35	0.100	0.34	339	1.40E+05	4.06	0.34	0.0324
16	0.11	2.32	0.127	0.39	49	2.00E+03	30.23	7.33	0.2109
17	0.11	2.32	0.127	0.39	102	8.57E+03	15.77	2.23	0.1088
18	0.11	2.32	0.127	0.39	171	2.40E+04	9.67	1.00	0.0714
18A[†]	0.11	2.32	0.127	0.39	171	2.40E+04	9.67	1.00	0.0238
18B[†]	0.11	2.32	0.127	0.39	171	2.40E+04	9.67	1.00	0.2143
19	0.11	2.32	0.127	0.39	271	6.00E+04	5.55	0.50	0.0499
20	0.11	2.32	0.127	0.39	383	1.20E+05	4.00	0.29	0.0397

Table 1. Parameters of simulated ISWs. In all cases, $h_{pyc}/H = 0.02$ and $\Delta\rho/\rho_0 = 0.8$. Boundary-layer thickness measures, δ_s and δ_v are scaled by the largest roughness height simulated $h_{b_0}/H = 10^{-3}$. For each ISW (i.e. each row, excluding cases A and B), four simulations were conducted with different bottom roughness (80 simulations): $h_b/H = 10^{-3}$, $h_b/H = 10^{-4}$, $h_b/H = 10^{-5}$ and $h_b/H = 0$ (flat bottom). [†]Cases A and B were simulated to investigate the effect of roughness wavelength and only considered $h_b/H = 10^{-3}$ and $h_b/H = 10^{-4}$ (16 simulations). A total of 96 simulations were conducted.

which represents a pycnocline of half-thickness h_{pyc}, centred at depth z_{pyc}, with z positive upwards. In all cases, $h_{pyc}/H = 0.02$ and $\Delta\rho/\rho_0 = 0.8$.

Due to the streamwise variability of the BBL flow, boundary-layer parameters varied in the streamwise direction (figure 2c). For scaling purposes, we defined the boundary-layer thickness representative of each ISW (δ_s) as the height of the 99% free-stream velocity (δ_{99}) at the ISW trough, where $U_\infty = U_2$. The viscous sublayer thickness representative of each ISW (δ_v), was defined as the minimum value of the laminar sublayer height $5\frac{\nu}{u_*}$ upstream of the separation point, which is the region of the BBL where the flow was unstable. In figure 2(c), values of $5\nu/u_*$ are only shown upstream of x_{sep} because $5\nu/u_* \to \infty$ as $x \to x_{sep}$ (because $u_* \to 0$). Here, u_* is the friction velocity and τ_b is the wall shear stress, both varying in the streamwise direction and defined as

$$u_*(x) = \left(\frac{\tau_b}{\rho_0}\right)^{1/2}, \qquad \tau_b(x) = \nu\rho_0\left(\frac{\partial u}{\partial z}\right)_{z=0}. \tag{2.2}$$

2.2. *Numerical model and simulation set-up*

The 2-D numerical simulations were conducted with the pseudospectral code SPINS (Subich *et al.* 2013). SPINS solves the 2-D incompressible Navier–Stokes equations under the Boussinesq approximation

$$\frac{\partial u}{\partial t} + u\frac{\partial u}{\partial x} + w\frac{\partial u}{\partial z} = -\frac{1}{\rho_0}\frac{\partial p}{\partial x} + \nu\nabla^2 u, \tag{2.3}$$

$$\frac{\partial w}{\partial t} + u\frac{\partial w}{\partial x} + w\frac{\partial w}{\partial z} = -\frac{1}{\rho_0}\frac{\partial p}{\partial z} + \nu\nabla^2 w - \frac{\rho g}{\rho_0}, \tag{2.4}$$

$$\frac{\partial \rho}{\partial t} + u\frac{\partial \rho}{\partial x} + w\frac{\partial \rho}{\partial z} = \kappa\nabla^2\rho, \tag{2.5}$$

$$\frac{\partial u}{\partial x} + \frac{\partial w}{\partial z} = 0, \tag{2.6}$$

where (x, z) are the horizontal and vertical coordinates, (u, w) are the associated velocity vectors, t is time, p is the pressure, ρ is the fluid density and κ is the molecular diffusivity. For all cases, the simulated $Pr = \nu/\kappa = 1$.

SPINS implements a spectral collocation method for the simulation of the stratified Navier–Stokes equations in rectilinear and smooth curvilinear geometries. To solve for curvilinear geometries, the model defines a terrain-following grid in the physical space, which is mapped to a rectangular computation domain (see for more details Subich *et al.* 2013). The model solves the equations in the computational box and then maps the solution back to physical coordinates. The spectral accuracy in conjunction with a curvilinear geometry makes SPINS unique and suitable for the study of boundary-layer instability of stratified flows over non-flat-bottom boundaries. For the no-slip boundary condition (b.c.), the model implements Chebyshev polynomials with a Chebyshev–Gauss–Lobatto quadrature grid that clusters the grid points near the walls, suitable to resolve the boundary-layer dynamics. Recent studies have shown the capability of the model to solve nonlinear internal wave problems, at laboratory scales, to investigate wave–boundary interaction (Deepwell *et al.* 2021; Hartharn-Evans *et al.* 2022), boundary-layer instability (Harnanan *et al.* 2017; Posada-Bedoya *et al.* 2024) and sediment resuspension (Olsthoorn & Stastna 2014).

In the present set-up, no-slip and no-flux boundary conditions were imposed on the top and bottom boundaries, with periodic horizontal boundary conditions (figure 2a). A Chebyshev–Gauss–Lobatto grid was employed in the vertical direction with a clustering of grid points near the top and bottom walls and a uniform grid was used in the horizontal direction. Grid resolution was defined to solve at least 15 points per roughness wavelength in the horizontal direction, and at least 7 Chebyshev grid points below the roughness height, i.e. below $z = h_b$. These grid resolutions are comparable to those used by Carr *et al.* (2010) to resolve the corrugated bed, and by Stastna & Lamb (2008) to resolve the flow surrounding bottom topography. The terrain-following coordinates used by the numerical model relax the grid requirements because of the exact definition of the boundary conditions following the variable bottom. Grid resolutions ranged from 2048×256 to 8192×4096 in the horizontal and vertical directions respectively. We conducted additional simulations doubling the grid resolution in both directions for selected cases to verify grid independence at these resolutions (Appendix A). From these,

we verified grid independence down to 3 grid points below $z = h_b$ and 8 grid points per roughness wavelength.

2.3. *Parameter space*

We conducted an extensive parametric study that explored the effect of changes in ISW-induced BBL parameters Re_{ISW}, P_{ISW}, and roughness parameters h_b and λ_b on the nature of the BBL instability. We considered 20 different ISWs over the Re_{ISW} versus P_{ISW} space (figure 1). To investigate the effect of roughness on the BBL instability, we analysed separately the effect of changing the roughness height, while keeping the roughness wavelength constant for each ISW, and *vice versa*. A total of 96 simulations were carried out for this study: 80 out of the 96 simulations varied the roughness height while keeping the same wavelength for each ISW; the remaining 16 simulations were selected cases to investigate the effect of varying the roughness wavelength.

2.3.1. *Roughness height*

For each ISW we simulated a flat-bottom case ($h_b/H = 0$) and three roughness heights: $h_b/H = 10^{-3}$, $h_b/H = 10^{-4}$ and $h_b/H = 10^{-5}$. For a laboratory-scale 1 m deep tank, these correspond to 1, 0.1 and 0.01 mm respectively, which are close to representative roughness scales of typical flume materials (Darby & Chhabra 2017); 0.001 mm–0.01 mm for glass ($h_b/H = 10^{-5}$) and 0.025 mm–0.2 mm for smooth concrete ($h_b/H = 10^{-4}$). For rough concrete and imperfections, for example, caulking used for joining glass panels, or when considering a sediment bed (e.g. Aghsaee & Boegman 2015; Ghassemi *et al.* 2022) roughness can be $\sim \mathcal{O}(1)$ mm, represented here by the cases with $h_b/H = 10^{-3}$.

To investigate the effect of roughness height, the roughness wavelength was kept constant for each ISW case. We set the roughness wavelength equal to the wavelength of the most unstable mode of the BBL (λ_b^{OS}) predicted by linear stability theory (see § 2.4). Therefore, we considered optimal conditions for the roughness elements to favour growth of instabilities in the BBL, as has been shown for surface periodic waves (Blondeaux & Vittori 1994) and SSWs (Scandura 2013). By analysing different ISWs over the (Re_{ISW}, P_{ISW}) space, this definition of λ_b allowed us to compute the most unstable (Re_{ISW}, P_{ISW}) for a given h_b, as often done to define thresholds of BBL instability (e.g. Schlichting 1968; Verschaeve & Pedersen 2014). This was a more consistent approach than, for example, arbitrarily selecting '*a priori*' a constant roughness wavelength for all ISWs, or considering random roughness, which would make it more difficult to parametrically investigate the effect of roughness wavelength on the BBL instability. Complementary laboratory experiments (unpublished, in preparation) of periodic ISWs propagating over a deformable sediment bed showed that bedforms develop with a characteristic wavelength that matches that of the most unstable mode of the BBL, which also motivated our definition of λ_b. In the discussion section, we will show that the conclusions drawn here, based on the parametric definition of the roughness wavelength, remain valid and can be extended to more realistic roughness conditions.

2.3.2. *Roughness wavelength*

To investigate the effect of roughness wavelength, we repeated the simulations with two additional roughness wavelengths for selected ISWs (cases 3, 8, 13 and 18 in table 1). These additional simulations were only repeated for $h_b/H = 10^{-3}$ and 10^{-4}. The additional roughness wavelengths were chosen far from the initially simulated wavelength of the most unstable mode: $\lambda_b^- = \lambda_b^{OS}/3$ and $\lambda_b^+ = 3\lambda_b^{OS}$, considering that λ_b^- is limited by the horizontal grid resolution.

The parameters of the simulated ISWs and their associated BBLs are summarized in table 1. Figure 1 illustrates the selected ISWs in the Re_{ISW} versus P_{ISW} and a/H versus Re_w parameter space, along with the corresponding experiments by Carr *et al.* (2008) and Zahedi *et al.* (2021). The simulations were designed to cover the range of parameters encompassing the various numerical and experimental instability thresholds. This allowed us to investigate the effects of bottom roughness on the different instability parameterizations.

2.4. *Space–time linear stability analysis*

We conducted a space–time linear stability analysis to: (*a*) determine the wavelength of the most unstable mode for each ISW, which was set as the roughness wavelength in our simulations (see § 2.3.2), and (*b*) compute the total linear spatial amplification in the BBL beneath each ISW, which was analysed in conjunction with the thresholds of instability predicted by our simulations.

For each ISW, we analysed the stability properties of the reverse-flow jet within the separated BBL (i.e. upstream of the separation point) in the frame of reference of the progressive ISW. The velocity profiles were uniformly sampled behind the ISW trough, from the 2-D flat-bottom simulations, at a time prior to the onset of instability – if observed. For each velocity profile $U(z)$, we solved the Orr–Sommerfeld (O–S) equation (Drazin & Reid 1981)

$$\frac{i}{Re}\left(\frac{d^4\hat{v}}{dz^4} - 2\alpha^2\frac{d^2\hat{v}}{dz^2} + \alpha^4\hat{v}\right) - (\alpha U(z) - \omega)\left(\frac{d^2\hat{v}}{dz^2} - \alpha^2\hat{v}\right) - \alpha\frac{d^2U(z)}{dz^2}\hat{v} = 0, \quad (2.7)$$

with boundary conditions

$$\hat{v}(0) = \frac{d\hat{v}}{dz}(0) = 0, \quad \hat{v}(z \to \infty) \to 0, \quad \frac{d\hat{v}}{dz}(z \to \infty) \to 0. \quad (2.8)$$

We determined the set of complex frequencies $\omega = \omega_r + i\omega_i$ associated with a corresponding given set of complex wavenumbers $\alpha = \alpha_r + i\alpha_i$ for perturbations with the general form

$$v' = \hat{v}(z)e^{i(\alpha x - \omega t)}. \quad (2.9)$$

Under this approach, ω_r and α_r represent the frequency and wavenumber of the linear instability, and ω_i and $-\alpha_i$, respectively, represent the growth (time) and amplification (space) rate; where we make the distinction between growth in time and amplification in space. Equation (2.7) was solved using a Chebyshev collocation method (Orszag 1971). Further details of the Orr–Sommerfeld equation solution and its validation are presented in Appendix B.

The Orr–Sommerfeld equation assumes steady, incompressible and parallel base flow $U(z)$. The stability analysis was conducted in the frame of reference of the ISW, where the inviscid flow imposed on the inner layer was steady (e.g. Verschaeve & Pedersen 2014; Posada-Bedoya *et al.* 2024). The flow in the inner layer is quasi-steady because the rate of change within the inner layer is sufficiently low or close to the reference frame of the solitary wave. Non-parallel effects can be expected to be weak in shallow laminar separated flows (Diwan & Ramesh 2012), with a small aspect ratio (i.e. height-to-length ratio, h_b/L_b). For this reason, local parallel stability theory works well for laminar separation bubbles (e.g. Marxen *et al.* 2003). In our simulations, the aspect ratios of streamlines, in the separation region ($h_b/L_b \approx 0.02 - 0.04$) (e.g. compare x and z
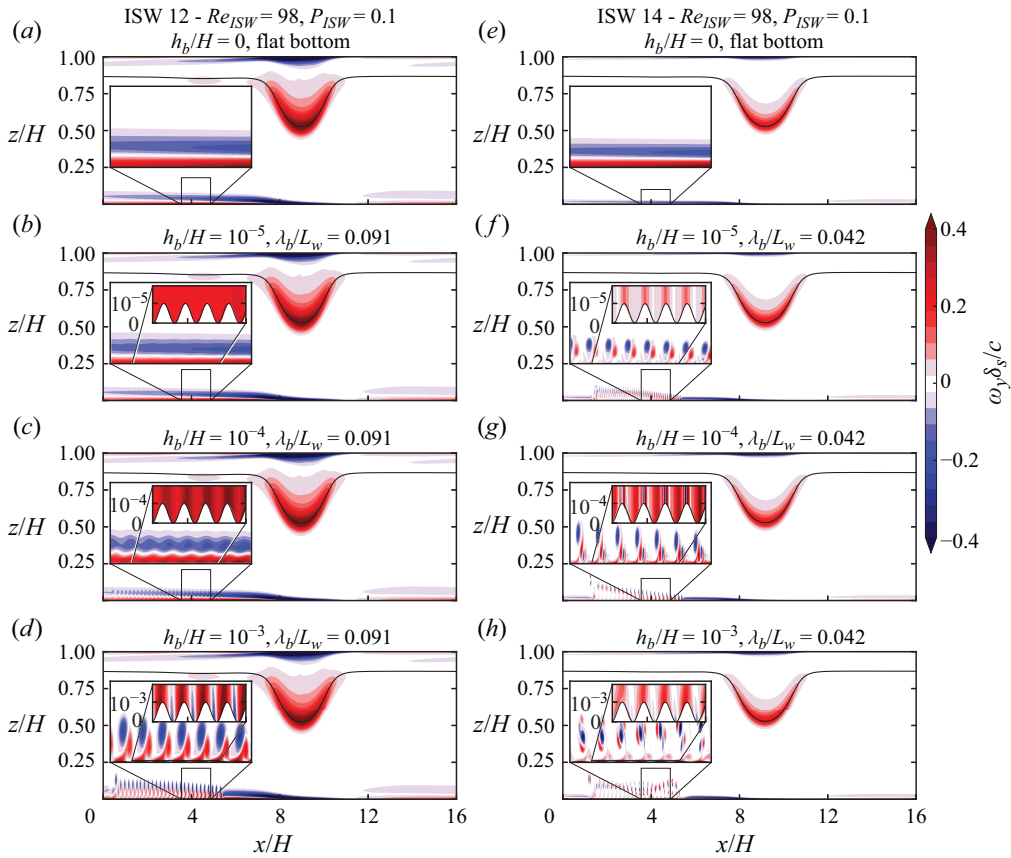
Figure 3. Snapshots of the non-dimensional vorticity field ($\omega_y \delta_s/c$) after the ISW passage over (a,e) the flat bottom and the rough wall region with three simulated roughness heights: (b,f) $h_b/H = 10^{-5}$, (c,g) $h_b/H = 10^{-4}$, (d,h) $h_b/H = 10^{-3}$. Results for two selected ISWs with $P_{ISW} = 0.1$: (a,b,c,d) $Re_{ISW} = 98$ and (e,f,g,h) $Re_{ISW} = 240$. Cases correspond to ISW 12 and 14 in table 1, respectively. For each ISW, the roughness wavelength was the wavelength of the most unstable mode of the BBL (see λ_b^{OS}/L_w in table 1). Each panel shows a near-bed zoom of the vorticity field over the rough wall region and a zoom of the bottom topography. Note that the domains here are shifted to the right from the schematic in figure 2.

scales in figure 2(c)), are within typical values reported in the literature (see figure 3a in Diwan & Ramesh (2012)) and so we can invoke the arguments of Diwan & Ramesh (2012) to consider a locally parallel BBL, suitable for local linear stability analysis.

We iteratively solved (2.7) for each flat-bottom simulated ISW velocity profile to obtain 2-D maps of (ω_r, ω_i) as a function of selected sets of (α_r, α_i); similar to Jones *et al.* (2008). The values of ω_i along (α_r, $\alpha_i = 0$) correspond to the solution of the temporal problem of the O-S equation, which predicts the spectrum of growth rates for a set of real wavenumbers α_r. Likewise, the values of $-\alpha_i$ along (ω_r, $\omega_i = 0$) correspond to the solution of the spatial problem of the O-S equation, which predicts the spectrum of amplification rates ($-\alpha_i$) for a set of real frequencies ω_r. Figure 14 in Appendix C shows an illustrative example of the 2-D map and the corresponding spectra of growth and amplification rates for a selected velocity profile. This procedure was repeated for

each velocity profile sampled behind each ISW trough. Note that this spatial-temporal 2-D mapping is often conducted when looking for the presence of convective or absolute instability through the cusp-map technique (Kupfer *et al.* 1987; Schmid & Henningson 2001).

2.4.1. *Most unstable wavelength*

For each ISW, we defined a corresponding wavelength representative of the most unstable spatial mode (i.e. largest $-\alpha_i$), λ_b^{OS}, which was set as the wavelength of the periodic roughness in our 2-D simulations. Given the weak streamwise variability of the BBL flow, the computed most unstable wavelength slightly varied in the streamwise direction. To define a single wavelength representative of the most unstable mode of each BBL, λ_b^{OS} was computed as the weighted average of the most unstable wavelengths over the pocket of local instability, with amplification rate as the weighing factor. For selected cases, we verified that the BBL instability, predicted by the 2-D simulations, was not significantly sensitive to variations in λ_b^{OS} within $\pm 10\%$; likely due to the continuous spectrum of unstable modes. Values of λ_b^{OS} are summarized in table 1.

2.4.2. *Amplification factor*

We followed the approach of Verschaeve & Pedersen (2014) to compute the spatial amplification of the linear instability beneath the ISW. The amplitude ratio of the instability ($A = A(x)$) relative to the unknown but small value A_0 at the separation point x_{sep} (where the region of instability begins, see figure 2(*c*)) was computed

$$\log_{10}\left(\frac{A}{A_0}\right) = -\int_{x_{sep}}^{x} \alpha_i(x)\mathrm{d}x. \tag{2.10}$$

Here, $-\alpha_i(x)$ is the amplification rate of the most unstable mode computed for each selected velocity profile (i.e. at each location x). This approach is known as the N-factor method (Herbert 1997), where the N factor is given by the maximum amplitude ratio in the streamwise direction

$$N = \max\left(\log_{10}\frac{A}{A_0}\right). \tag{2.11}$$

Results of the N-factor method are presented in § 3.3.

3. Results

3.1. *Roughness-induced BBL instability*

For brevity, we focus the description on selected illustrative ISW cases. A similar dependence of the BBL stability on the roughness parameters was identified for all ISWs in the parameter space.

3.1.1. *Effect of roughness height*

To show the effects of roughness height, we describe the production of vortex-shedding for ISW 12 ($Re_{ISW} = 98$, $P_{ISW} = 0.1$) and ISW 14 ($Re_{ISW} = 240$, $P_{ISW} = 0.1$). These were chosen because they were both expected to be stable and remained laminar when the ISW passed over the flat-bottom region in our simulations (figure 3a,e), in agreement with the 2-D simulation-derived threshold formulated by Aghsaee *et al.* (2012). However, for the $Re_{ISW} = 240$ case, the BBL was expected to be unstable according to the laboratory experiments by Carr *et al.* (2008) and Zahedi *et al.* (2021) (figure 1).

To visualize the effects of varying the roughness height on the production of near-bed vortex shedding, figure 3 shows the vorticity for these cases. The roughness wavelength was equal to that of the most unstable mode of the reverse-flow jet predicted by the O-S equation from the associated flat-bed case (see 2.3.1 and table 1).

For $Re_{ISW} = 98$ the amplitude of the near-bed vorticity field perturbations increased with increasing roughness height. However, vortex shedding only occurred for $h_b/H = 10^{-3}$ ($h_b/\delta_v = 0.44$) (figure 3d). For $h_b/H = 10^{-4}$, the roughness elements introduced instabilities in the near-bed vorticity field, but these were not sufficient to trigger vortex shedding (figure 3c). Rather, the roughness-induced instabilities decayed after the passage of the ISW. For $h_b/H = 10^{-5}$, the perturbations were much smaller and the BBL flow was nearly insensitive to the roughness, closely resembling the laminar flat-bottom case (cf. panels *a* and *b* in figure 3).

For $Re_{ISW} = 240$, the BBL was stable over the flat-bottom, but vortex shedding occurred over the rough wall region for the three simulated roughness heights (figure 3f–h), even for $h_b/H = 10^{-5}$, which was two orders of magnitude smaller than the viscous sublayer thickness: $h_b/\delta_v = 0.017$. This result clearly shows that small-scale roughness, characteristic of smooth flume materials, is a BBL destabilizing mechanism beneath ISWs.

Vortex shedding occurred earlier for larger roughness heights (cf. panels *f–h* in figure 3). For $h_b/H = 10^{-3}$, vortices detached completely and moved away from the wall over the entire rough wall region. In comparison, for $h_b/H = 10^{-4}$ and $h_b/H = 10^{-5}$, the roughness-induced instability was still transitioning after the same elapsed time, with vortices forming near the front end of the rough wall region; thus showing differences in the vertical position of the vortices along the rough bed. Therefore, increasing the roughness height increases the amplitude of the seeding perturbations, thereby facilitating the transition toward vortex shedding.

The nature of the BBL stability does not only respond to changes in bottom roughness but also depends on the ISW-induced BBL parameters Re_{ISW} and P_{ISW}. For example, ISW 12 over $h_b/H = 10^{-4}$ (figure 3c) and ISW 14 over $h_b/H = 10^{-5}$ (figure 3f) had similar values of h_b/δ_v; 0.044 and 0.017, respectively. However, the BBL stability was different between these cases, with only ISW 14 triggering vortex shedding. This difference in vortex shedding between different Re_{ISW} at similar h_b/δ_v shows that vortex shedding of the BBL, in response to the bottom roughness, is not solely dependent on h_b/δ_v.

A similar response to changes in roughness height occurred for all waves in the parameter space, with vortex shedding being triggered for a critical h_b that varied depending on Re_{ISW} and P_{ISW}, as we discuss later.

3.1.2. *Effect of roughness wavelength*

To illustrate the effects of roughness wavelength on BBL instability, we considered ISW 3 and ISW 13 (table 1) propagating over roughness with three different wavelengths and the same $h_b/H = 10^{-4}$ (see § 2.3.2). The roughness wavelengths (λ_b^{OS}, $\lambda_b^- = \lambda_b^{OS}/3$ and $\lambda_b^+ = 3\lambda_b^{OS}$) were defined based on spectra of the growth and amplification rates for velocity profiles of the reverse-flow jet within the separated BBL (figure 4) (see § 2.3.2).

The simulations (figure 5) support the conclusion that roughness wavelength is a crucial parameter for the stability of the BBL. For the shortest λ_b^- and longest λ_b^+, vortex shedding did not occur, except for localized instabilities at the edges of the rough wall region (panels *a,c* and *d,f*). We attribute those instabilities to the discontinuity in the second derivative of the topography at the transition flat to rough. As the flow at the edges of the roughness
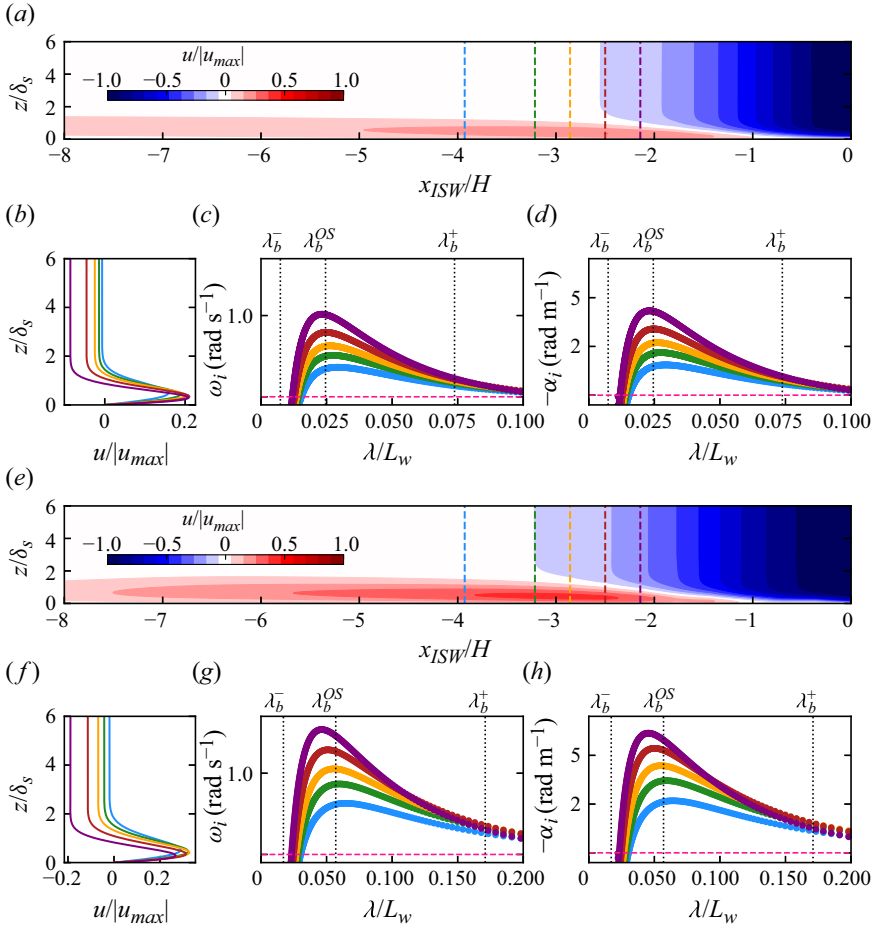
Figure 4. (*a,e*) Snapshots of the near-bed horizontal velocity from simulations of two selected ISWs propagating over a flat bottom. The waves are visualized in the ISW frame of reference, with $x_{ISW} = 0$ at the ISW trough. (*b,f*) Selected near-bed velocity profiles of the separated BBL in the flat-bottom simulation for the two selected ISWs. Locations of the profiles are indicated by corresponding coloured vertical dashed lines in panels (*a*) and (*e*), respectively. (*c,g*) Growth rate (ω_i) and (*d,h*) amplification rate ($-\alpha_i$) spectra of unstable modes for each selected velocity profile. Panels show (*a,b,c,d*) ISW 3 ($Re_{ISW} = 177$, $P_{ISW} = 0.044$) and (*e,f,g,h*) ISW 13 ($Re_{ISW} = 170$, $P_{ISW} = 0.1$). Vertical dotted lines in panels (*c,d,g,h*) indicate the roughness wavelength in the three simulated cases.

region is different from the flow over the periodic bumps, the latter being the focus of the present study, the instabilities at the edges of the rough wall region are inconsequential for the present analysis. Conversely, BBL instability and uniform vortexshedding, over the rough wall region, occurred when the roughness wavelength matched that of the most unstable mode of each BBL (panels *b* and *e*). This result suggests that the BBL beneath ISWs behaves as a resonator, with a tendency to preferably amplify perturbations with a wavenumber closer to that of the most unstable mode of the BBL flow. The amplification and vortex shedding are more energetic for cases with larger growth/amplification rates predicted by linear stability theory (cf. panels *c,d* versus *g,h* in figure 4). In the discussion section, we present additional simulations using random roughness to further explore the role of roughness wavelength on instability amplification.
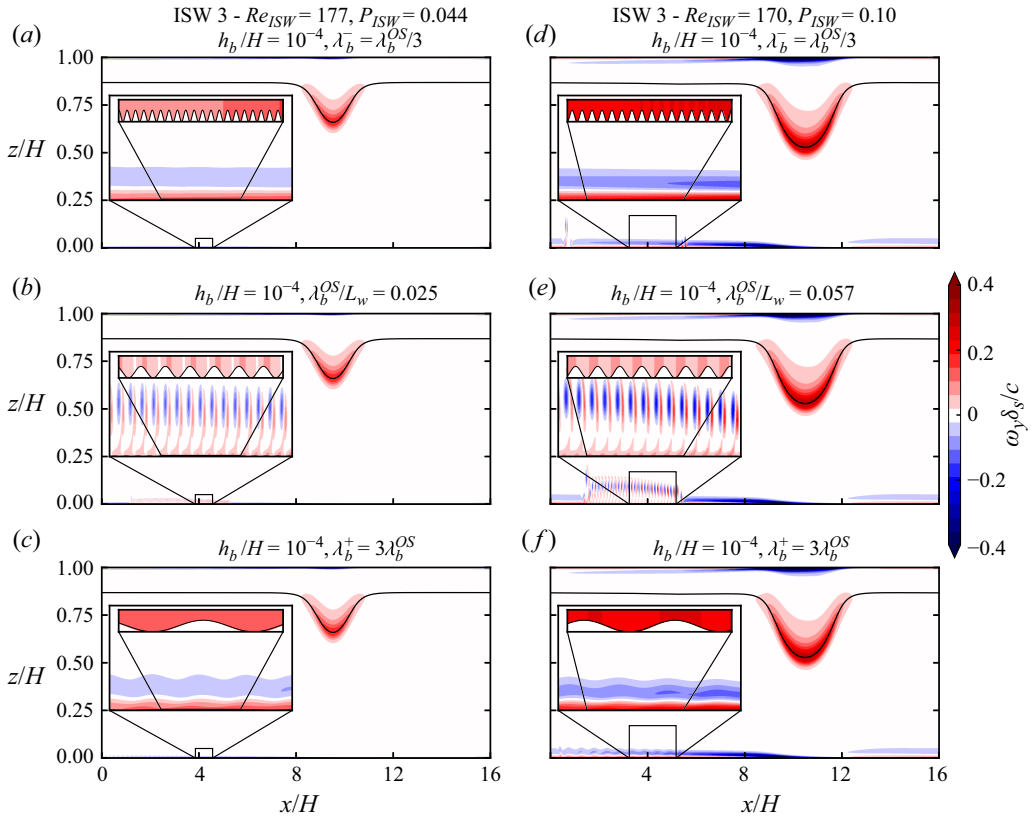
1009 A21-14

Figure 5. Snapshots of the non-dimensional vorticity field ($\omega_y \delta_s / c$) after the ISW passage over the rough wall region for two selected ISWs: (a,b,c) ISW 3A, 3 and 3B ($Re_{ISW} = 177$, $P_{ISW} = 0.044$), respectively, and (d,e,f) ISW 13A, 13 and 13B ($Re_{ISW} = 170$, $P_{ISW} = 0.1$), respectively. All the cases had the same roughness height $h_b / H = 10^{-4}$. For each ISW, three different roughness wavelengths were simulated: (a,d) $\lambda_b^- = \lambda_b^{OS}/3$, (b,e) λ_b^{OS}/L_w, (c,f) $\lambda_b^+ = 3\lambda_b^{OS}$ (see table 1). Each panel shows a near-bed zoom of the vorticity field over the rough wall region and a zoom of the bottom topography. Note that the domains here are shifted to the right from the schematic in figure 2.

3.2. *Bottom boundary layer instability amplification mechanisms*

We have shown that changes in both roughness height and wavelength modify the stability of the ISW BBL and provide a path for vortexshedding, in an otherwise stable flow over a flat bottom. We have identified two different vortex-shedding mechanisms for $h_b / \delta_v \approx 1$ and $h_b / \delta_v \approx 10^{-1}$. Here, we describe the instability amplification mechanisms, in more detail, over the rough wall region for ISW 13 ($Re_{ISW} = 170$, $P_{ISW} = 0.1$). A similar dynamics was observed for other ISWs, but with differing amplification and vortex-shedding rates depending on the set Re_{ISW}, P_{ISW}, h_b and λ_b.

For the case of $h_b / \delta_v \approx 1$, as the ISW passed over the rough wall region, snapshots of the near-bed vorticity and streamlines show local flow separation at the aft of bumps close to the separation point of the BBL (figure 6). The local separation ejected the vortices out of the BBL. This destabilization and vortex shedding occurred early upon the ISW passage and were quite close to the separation point of the BBL, behind the ISW trough. The production of vortex-shedding was similar to the observations by Carr *et al.* (2010) over corrugated beds, which is more representative of ISW propagation over bottom topography as opposed to small-scale surface roughness.
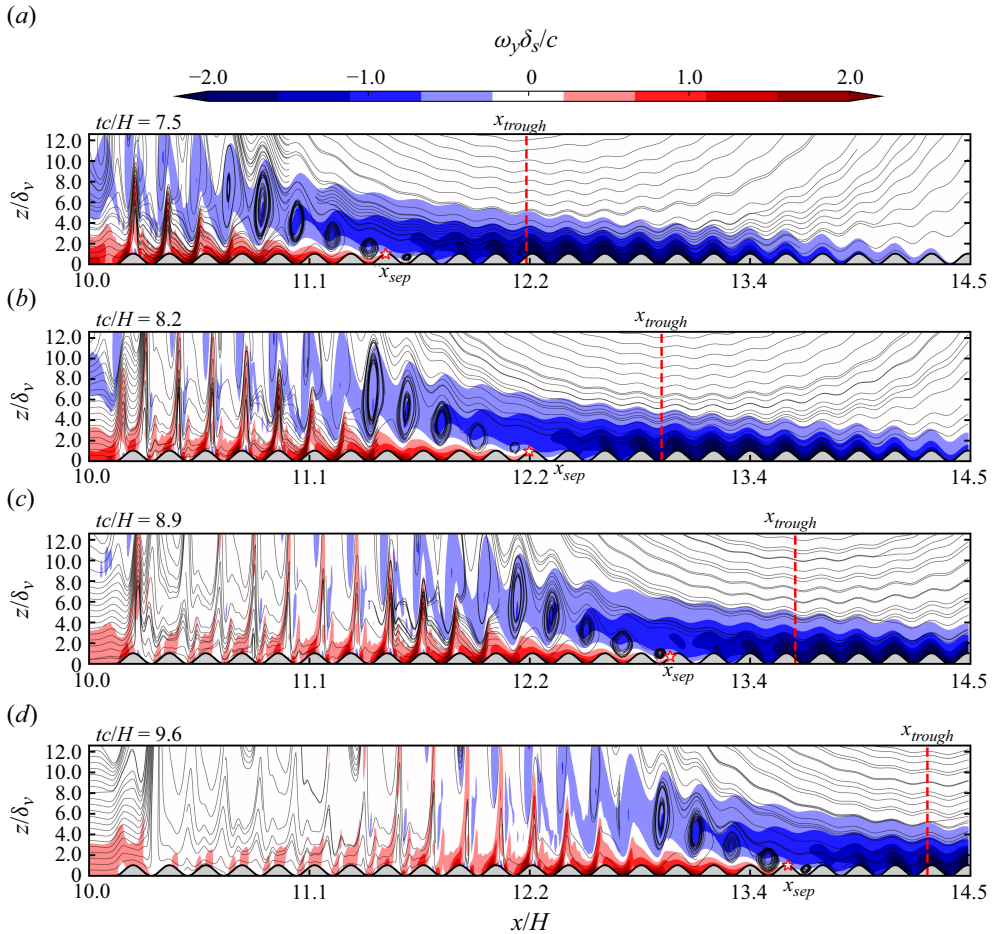
Figure 6. Snapshots of the non-dimensional vorticity field ($\omega_y \delta_s / c$) and streamlines during ISW passage over the rough wall region for ISW 13 with $Re_{ISW} = 170$, $P_{ISW} = 0.1$. The roughness height $h_b/H = 10^{-3}$ ($h_b/\delta_v = 1.03$). The vertical dashed line indicates the location of the ISW trough. The star indicates the location of the separation point.

For a significantly lower roughness height, with $h_b/\delta_v \approx 10^{-1}$, the BBL flow oscillated up and down with the roughness wavelength, without local separation or vortices at the aft of each bump (see figure 7). Rather, the effect of roughness was to seed perturbations in the BBL as fluctuations in the velocity field. The seed perturbations gradually grew with time, within the BBL, until they were of sufficient amplitude for nonlinear effects to become important. After further amplification, the instability field became steeper until streamlines overturned to form vortices that shed from the BBL. Therefore, the seed perturbations forced by small-scale roughness amplified over longer timescales and led to vortex shedding at later times that were farther behind the separation point, compared with $h_b/\delta_v \approx 1$.

For the smallest $h_b/\delta_v \approx 10^{-2}$, the same mechanism of roughness-induced noise and BBL amplification occurred, but the timing of the vortex shedding differed due to the smaller magnitude of the seed perturbations on the BBL (not shown). In the absence
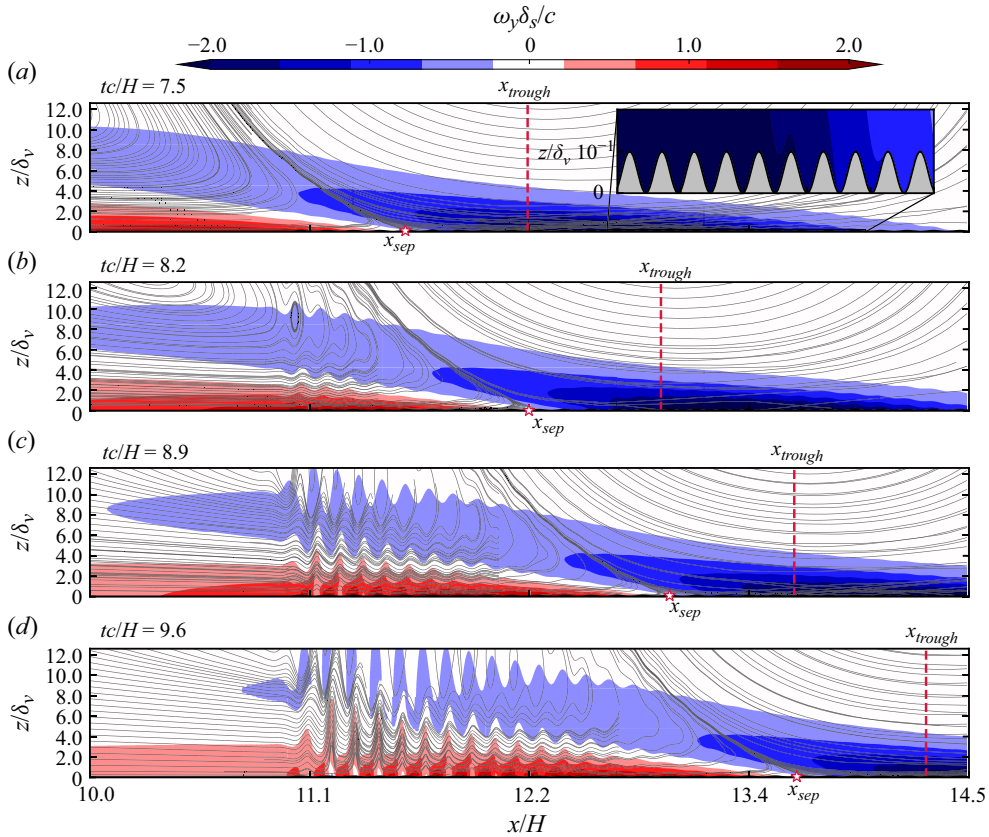
Figure 7. Snapshots of the non-dimensional vorticity field ($\omega_y \delta_s / c$) and streamlines during the ISW passage over the rough wall region for ISW 13 with $Re_{ISW} = 170$, $P_{ISW} = 0.1$. The roughness height $h_b/H = 10^{-4}$ ($h_b/\delta_v = 0.1$). The vertical dashed line indicates the location of the ISW trough. The star indicates the location of the separation point. Panel (a) contains an inset zoom of the bottom roughness elements.

of roughness, this ISW case remains stable. Therefore, it is expected that with a small enough roughness height, the total BBL amplification of the seed perturbations will be insufficient to overcome viscous damping and produce vortex shedding and the BBL will remain stable.

All cases simulated with $h_b/\delta_v \gtrsim 1$ led to vortex shedding with a phenomenology similar to that described for figure 6. However, even though for $h_b/\delta_v \lesssim 10^{-1}$ perturbations were always seeded within the BBL (e.g. figure 7), vortex shedding did not always occur. As described in § 3.1.1, vortex shedding of the ISW-induced BBL over roughness is not only dependent on h_b/δ_v, but also on the ISW-induced BBL parameters Re_{ISW} and P_{ISW}. This motivated us to investigate a roughness-induced vortex-shedding criterion, as described in the following sections.

3.3. *Amplification ratios*

The growth of BBL instabilities depends on how roughness perturbations are amplified in the wake of the ISW. As described in § 2.4.2, we computed the amplification ratio $\log_{10}(A/A_0)$ behind the wave trough for all ISWs from the linear stability analysis
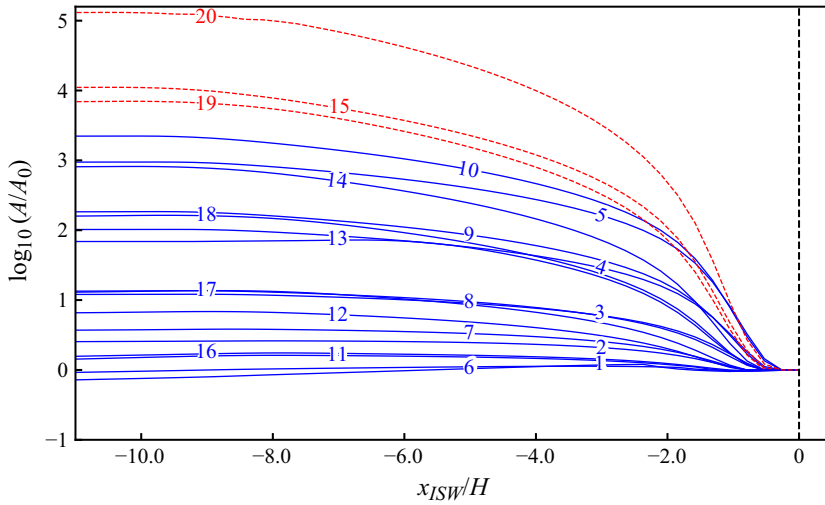
Figure 8. Amplitude growth curves behind the ISW trough for all simulated ISWs, in the ISW frame of reference, where x_{ISW} is the streamwise position in the ISW frame of reference, with abscissa zero at the ISW trough. Continuous blue and red dashed lines indicate stable and unstable BBL cases in the flat-bottom simulations respectively. In-line labels identify the ISWs in table 1.

using the N-factor method. We only used velocity profiles over the flat bottom, thereby representing the lowest amplification for each ISW case. We plot the amplification ratio behind the wave trough for all simulated ISWs in figure 8. The maximum asymptotic value in each curve corresponds to the amplification factor N, as defined in (2.11).

3.4. *Vortex-shedding threshold*

To summarize the effects of roughness on BBL stability over all of our simulations, we compared N with the experimental and numerical stability thresholds in Re_{ISW} versus P_{ISW} space (from figure 1). The stability threshold for our simulations, over the Re_{ISW} versus P_{ISW} space, was estimated for each roughness height and the flat-bottom case. In all simulations, the roughness wavelength was that of the most unstable mode for each ISW. Therefore, these thresholds must be interpreted as being associated with the most unstable (Re_{ISW}, P_{ISW}) for each h_b, as often done to define thresholds of BBL instability (e.g. Schlichting 1968; Verschaeve & Pedersen 2014). However, below, we show that more realistic random roughness also seeds the most unstable wavelength, validating the instability thresholds estimated here.

The discrete distribution of our simulated cases over the parameter space (figure 9) requires the computed thresholds of N to be defined as ranges of $N = N_c$. Hence, these thresholds were visualized as regions delimited by lines of constant $N = N_c$ that separate stable and unstable ISWs simulated for each h_b/H. Threshold regions shifted to the left, i.e. towards smaller Re_{ISW}, and to smaller values of $N = N_c$, as the roughness height increased. For $h_b/H = 10^{-3}$, the threshold region was roughly vertical, suggesting that the threshold is mostly determined by a critical $Re_{ISW} \approx 75$, with a weak dependence on P_{ISW}. For decreasing $h_b/H = 10^{-4}$, $h_b/H = 10^{-5}$ and $h_b/H = 0$, the N_c lines increased in slope, in the P_{ISW} versus Re_{ISW} space, suggesting an increasing dependence on P_{ISW} as h_b/H decreased and Re_{ISW} increased.
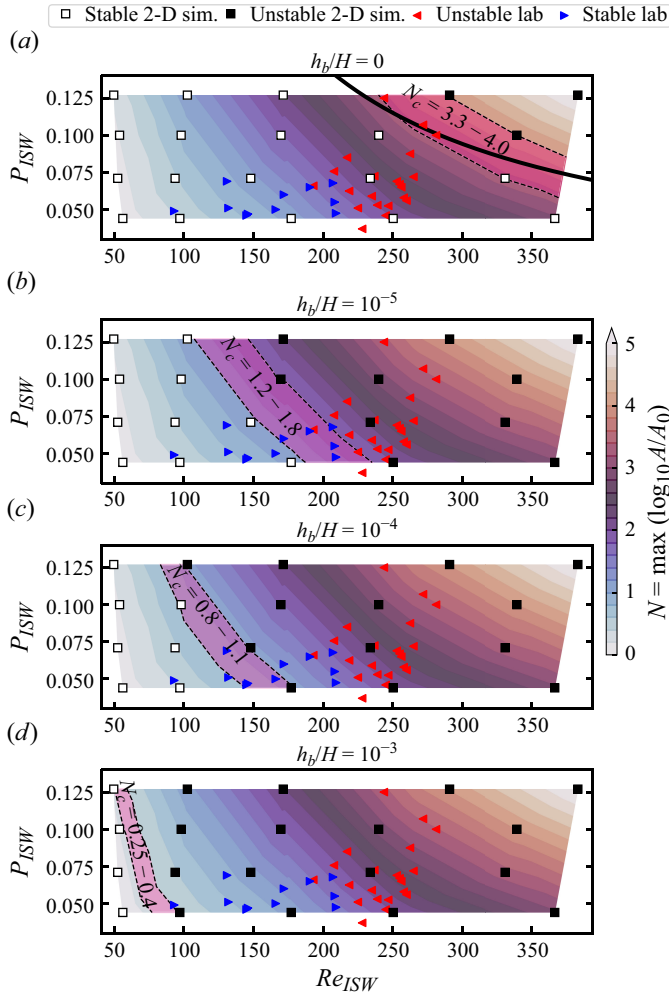
Figure 9. Stability diagrams in the P_{ISW} versus Re_{ISW} space for all simulated cases. Coloured contours represent the BBL amplification factor (N). (a) Flat bottom ($h_b/H = 0$), (b) $h_b/H = 10^{-5}$, (c) $h_b/H = 10^{-4}$ and (d) $h_b/H = 10^{-3}$. Pink-shaded regions delimited with black dashed lines indicate the approximated threshold regions associated with ranges of $N = N_c$.

In the flat-bottom case limit, only three cases were unstable in our simulations (ISWs 15, 19 and 20), with a critical $N_c \approx 3.3 - 4.0$ (see figure 9a), which is of similar order as the critical amplification estimated by Verschaeve & Pedersen (2014) (their figure 27) for the numerical simulations of Aghsaee *et al.* (2012). The observed instability is of the convective type, as previously described by Posada-Bedoya *et al.* (2024). The threshold region roughly matches the threshold curve proposed by Aghsaee *et al.* (2012) using 2-D spectral simulations. Discrepancies are likely due to their arbitrary selection of an equation to fit discrete stable and unstable cases (see their figure 12), which differed from our runs and also exhibited some uncertainty through the transition region. Overall, we consider that our 2-D flat-bottomed spectral simulations match the threshold of instability proposed by Aghsaee *et al.* (2012).

The threshold region for $h_b/H = 10^{-5}$ is the closest to the critical threshold ($Re_{ISW} \sim 200$, $P_{ISW} \sim 0.05 - 0.07$) associated with the laboratory experiments by Carr

et al. (2008) and Zahedi *et al.* (2021), with $N_c \approx 1.5 - 1.8$ (see figure 9*b*). This shows the critical amplification factor to be approximately two orders of magnitude smaller in the laboratory, compared with the 2-D flat-bottomed spectral simulations (both ours and those by Aghsaee *et al.* (2012)). This is quite close agreement to the estimates by Verschaeve & Pedersen (2014), which also report a difference of two orders of magnitude between the laboratory experiments by Carr *et al.* (2008) and the simulations by Aghsaee *et al.* (2012).

4. Discussion

We have shown that bottom roughness changes the stability of the BBL beneath ISWs of depression. The smallest roughness scale considered here, $h_b/H = 10^{-5}$, in some cases two orders of magnitude smaller than the viscous sublayer thickness, can destabilize the BBL and trigger vortex shedding, in an otherwise numerically stable BBL over a flat bottom. This roughness height is of the same order as in typical flume materials used in the laboratory (Darby & Chhabra 2017): 0.01–0.001 mm for glass and 0.2–0.025 mm for smooth concrete. Therefore, the dependence of the BBL stability on the characteristics of the small-scale surface roughness means that glass and smooth concrete should not be considered "smooth" surfaces in a laboratory setting of an ISW-induced BBL flow (see figure 9).

We identified two mechanisms for vortex shedding determined by the ratio h_b/δ_v. For $h_b/\delta_v \gtrsim 1$, vortices were forced directly by the local flow separation at the aft of each bump, more representative of ISW interaction with bottom topography (e.g. Carr *et al.* 2010). Conversely, for $h_b/\delta_v \lesssim 10^{-1}$, the presence of roughness forces the BBL to oscillate with the roughness wavelength, seeding perturbations in the BBL susceptible to being amplified by the BBL flow.

In both cases, amplification occurred preferably for roughness wavelengths close to those of the most unstable mode of the BBL, as predicted by linear instability theory. This resonator-like nature of the BBL flow beneath ISWs has also been reported for the BBL driven by SSWs (Scandura 2013) and periodic monochromatic waves (Blondeaux & Vittori 1994). Despite the similarities between the SSW and ISW problems, it remains a challenge to relate the stability of both BBL flows due to the additional parameters $\Delta\rho/\rho_0$ and z_{pyc}/H that define the ISWs (e.g. Verschaeve & Pedersen 2014).

4.1. *Vortex-shedding criterion: random roughness wavelength*

We have arbitrarily chosen the most unstable mode of the BBL as the roughness wavelength in our simulations. Given the resonator-like nature of the BBL, this can be considered the most favourable condition for roughness to destabilize the BBL. The thresholds computed above, therefore, correspond to the optimal and most unstable parameters Re_{ISW}, P_{ISW} that would destabilize the BBL for each h_b. To test the generality of these results, we performed simulations using more realistic random distributions of roughness wavelength.

Sixteen additional simulations were conducted to validate the generality of the thresholds in § 3.4. The selected cases were chosen from figure 9 immediately above and below the thresholds for $h_b/H = 10^{-4}$ and 10^{-5}. For each P_{ISW}, we chose the pair of cases with the largest stable Re_{ISW} and the smallest unstable Re_{ISW}, hence eight simulations per h_b/H (figure 10).

The random roughness is more representative of realistic beds measured in the laboratory (e.g. Sumer *et al.* 2010; Scandura 2013; Ghassemi *et al.* 2022). The rough bed was modelled as the superposition of sinusoids with a wide, nearly continuous spectrum
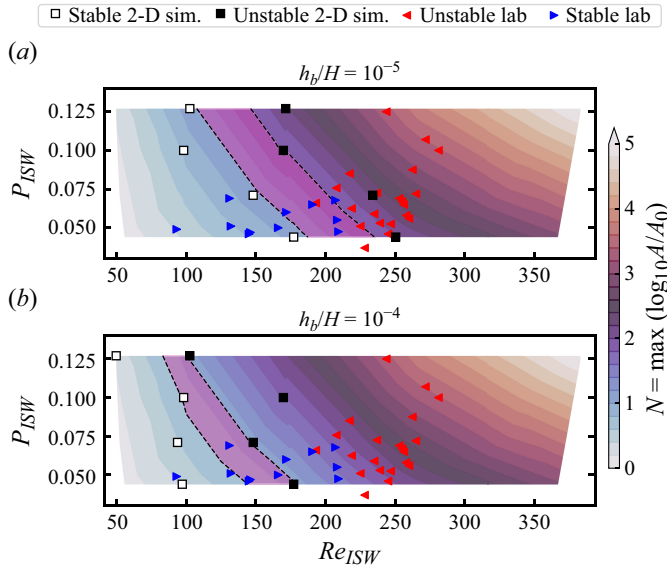
Figure 10. Stability diagrams in the P_{ISW} versus Re_{ISW} space for the sixteen cases simulated with random roughness wavelengths for (*a*) $h_b/H = 10^{-5}$, (*b*) $h_b/H = 10^{-4}$. Coloured contours represent the BBL amplification factor (N). Pink-shaded regions, delimited with black dashed lines, indicate the approximate threshold regions estimated from the sinusoidal roughness simulations (see figure 9).

of wavelengths, each with a definite random amplitude, as commonly done for random-roughness numerical studies (e.g. Stastna & Lamb 2008; Scandura 2013). The shortest modelled wavelength was limited by the grid resolution to 8 grid points. The modelled roughness is shown in figure 11(*e*), along with the band-pass-filtered signal associated with the most unstable wavelength of the BBL (spectral cutoff $(0.8–1.2)\lambda_b^{OS}$),which shows regions where the roughness shape follows the most unstable wavelength of the BBL.

To illustrate the BBL interaction with random roughness, figure 11 shows snapshots of the near-bed instantaneous vertical velocity as a selected ISW propagated over the random roughness region. Localized packets of vertical perturbations, behind the separation point, emanated from regions where the roughness had a dominant variability at the wavelength of the most unstable mode of the BBL (figure 11*a*–*d*). The seeded instability packets amplified over time and slowly moved downstream. At subsequent times, new instability packets formed from new regions where the separated BBL interacted with roughness dominated by the most unstable mode (figure 11*a*–*d*). As a consequence, the resulting envelope of the instability packets roughly followed the modulated amplitude of the band-pass-filtered roughness (cf. $w\,|_{\delta_s}\,/U_2$ versus band-pass-filtered roughness).

In all the sixteen cases, ISW propagation over random roughness predicted the same corresponding stability regimes (i.e. stable versus unstable, see figure 10) as the simulations with sinusoidal roughness. This indicates that the instability thresholds computed for sinusoidal roughness are valid for more realistic random roughness. This confirms that the BBL can resonate with the roughness as long as the random roughness field contains variance at the wavelength of the most unstable mode.

4.2. *Roughness-induced perturbations as seed noise*

For roughness elements completely within the viscous sublayer, we interpret BBL–roughness interaction as a mechanism for seeding perturbations in the BBL. Whether
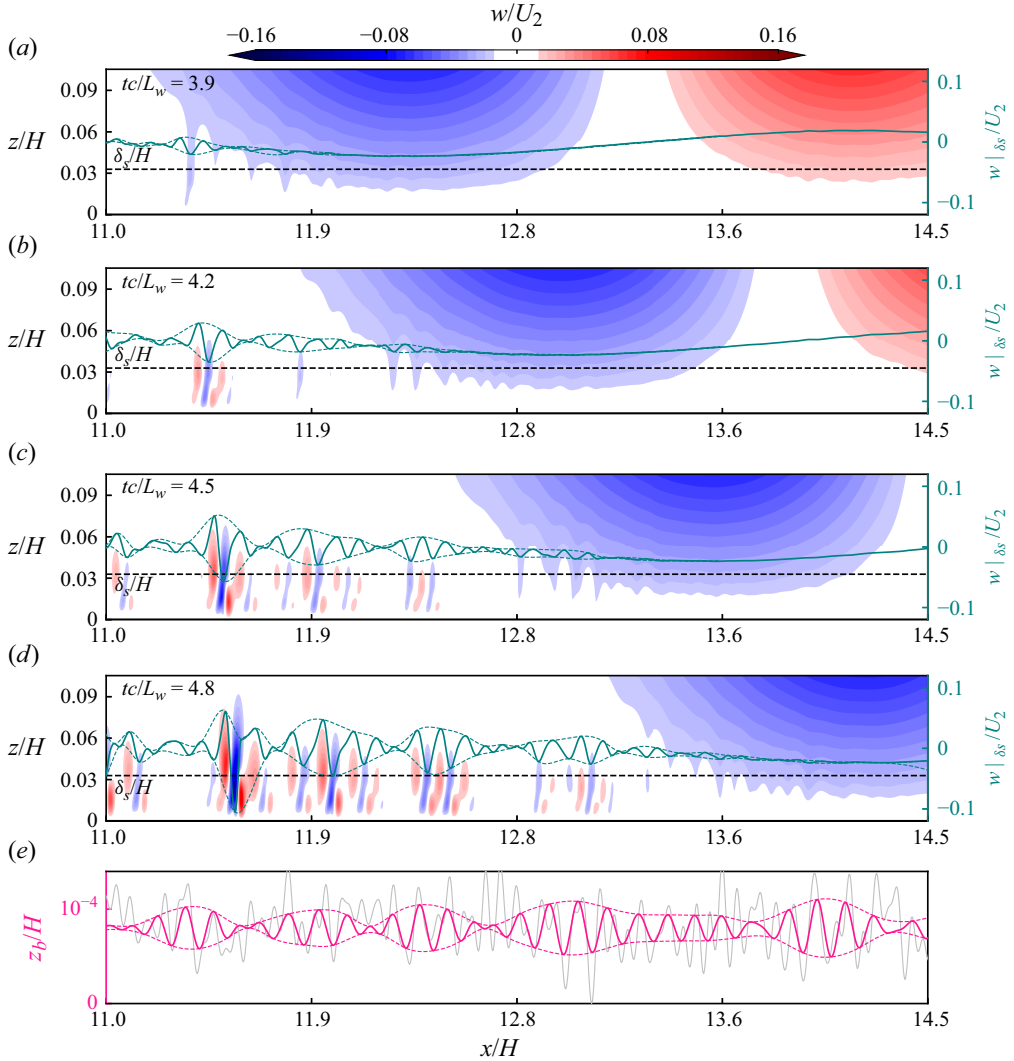
Figure 11. Snapshots of the instantaneous vertical velocity w/U_2 (filled contours) during propagation of ISW 13 (table 1) over the random roughness region at (*a*) $tc/L_w = 3.9$, (*b*) $tc/L_w = 4.2$, (*c*) $tc/L_w = 4.5$ and (*d*) $tc/L_w = 4.8$. Each panel shows a transect of w/U_2 at $z = \delta_s$ (black horizontal dashed line), with the associated scale on the right axis. The dashed lines indicate the upper and lower envelopes of the signal. (*e*) Random bottom roughness (grey line) and band-pass-filtered roughness (pink) around the wavelength associated with the most unstable mode of the BBL λ_b^{OS} (spectral cutoff $(0.8$–$1.2)\lambda_b^{OS}$). Dashed lines indicate the upper and lower envelopes of the band-pass-filtered signal.

these perturbations introduced by the roughness will be sufficiently amplified to eventually trigger vortex shedding depends on three parameters: (i) the initial amplitude (A_0) and (ii) the initial wavelength of the seed perturbations, and (iii) the amplification of the seed perturbations by the BBL flow (N). By considering roughness with the most unstable wavelength, we limited the search of critical instability parameters to A_0 and N. This is equivalent to computing the most unstable Re_{ISW} and P_{ISW} for each h_b.

Lines of constant amplification factor in the Re_{ISW} versus P_{ISW} space are consistent with the simulated separation between stable and unstable ISWs, with the threshold
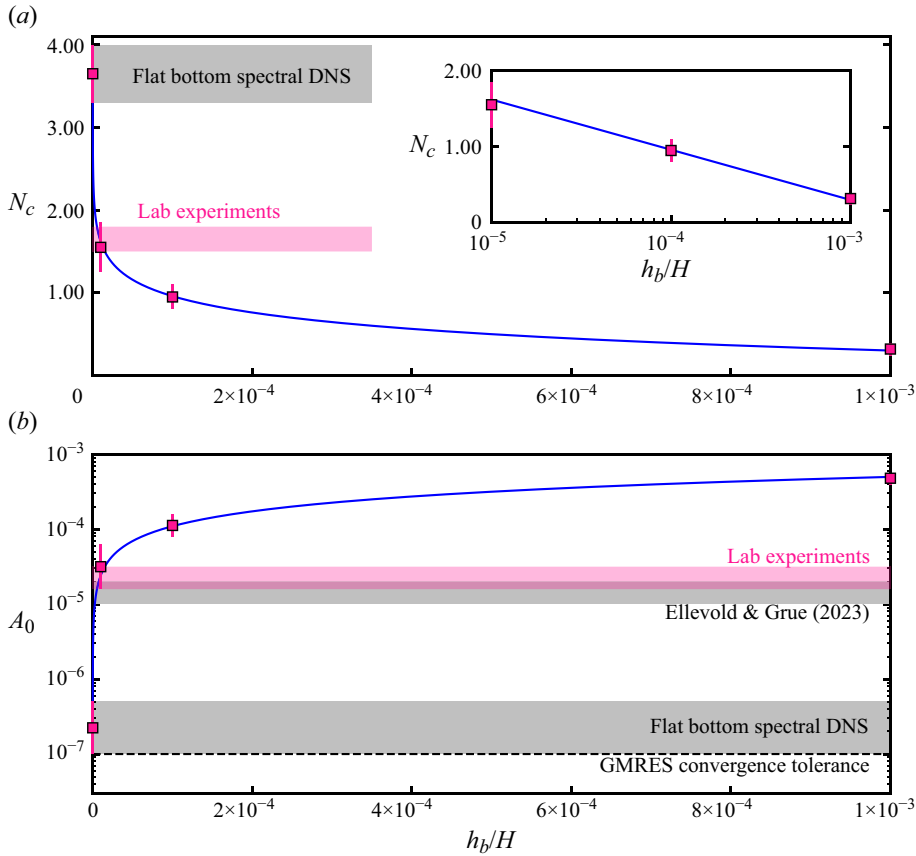
Figure 12. Ranges of (*a*) critical amplification factor (N_c) and (*b*) background noise amplitude (A_0) for the different roughness heights (h_b/H) and the flat-bottom simulations. Inset in panel (*a*) shows dispersion on a semilog *x*-axis, only including $h_b > 0$. Error bars correspond to the ranges of N_c (and associated A_0) for each threshold region defined in figure 9. Markers are placed in the middle of each range, and used to fit the curves. Shaded regions indicate the approximate range of N_c and noise levels (A_0) in the laboratory experiments, the present solver (approximately same as in the solver of Aghsaee *et al.* (2012)), and the finite-volume solver of Ellevold & Grue (2023). The dashed line in panel (*b*) indicates the convergence tolerance of the Generalized Minimum Residual (GMRES) algorithm in the flat-bottom simulations of the present study (10^{-7}).

shifting to smaller N_c and Re_{ISW} as h_b/H increased. By considering the most unstable roughness wavelength, the shifting of the instability thresholds to smaller N_c as h_b/H increased is equivalent to increasing the initial amplitude of the seed perturbations (i.e. A_0), such that smaller amplification is required to reach vortex shedding. Figure 12(*a*) shows the ranges of critical amplification associated with each threshold as a function of the roughness height. For finite h_b, the critical amplification N_c follows a logarithmic relation

$$N_c = -0.6579 \log_{10}\left(\frac{h_b}{H}\right) - 1.6718. \tag{4.1}$$

By demonstrating that roughness changes the stability characteristics of the BBL, we further hypothesize that our results can be generalized, by associating each roughness height with an equivalent level of seed noise. For the case of a Tollmien–Schlichting wave,

the threshold amplitude to trigger secondary instabilities lies at 1% of the free-stream velocity U_∞ (Herbert 1988; Verschaeve & Pedersen 2014). Here, we use the same 1% criterion for primary instability to trigger secondary instabilities. We assume $U_\infty \sim U_2$ and conduct the analysis based on the actual dimensional values of the simulated U_2. For our ISWs, $U_2 \approx 0.1$–0.2 m s^{-1} for all waves and so we define $U_\infty \sim 10^{-1}$ m s^{-1}. Assuming that the secondary instability is triggered once its amplitude has grown to $A \approx 0.01U_2$ in all cases, according to (2.10), $A_0 = 0.01U_2 10^{-N_c}$. Hence, we can estimate the background noise level A_0 associated with each N_c, which in turn is associated with each roughness height (figure 12a). Figure 12(b) shows the relation between h_b/H and the background noise level A_0 obtained through this procedure, which follows the relation

$$A_0 = 0.04697 \left(\frac{h_b}{H} \right)^{0.6579}. \tag{4.2}$$

The interpretation of roughness-induced perturbations as noise stems from the description of the BBL–roughness interaction in figure 7, where the BBL is forced to oscillate following the bottom roughness elements, introducing perturbations in the velocity field analogous to noise. From this perspective, for sinusoidal geometry, we can estimate the vertical velocity fluctuations that build the noise as

$$\text{Noise} \sim w' \sim \frac{2h_b}{\lambda_b} u_{jet}, \tag{4.3}$$

where u_{jet} is the velocity of the reverse-flow jet where the BBL flow is unstable; roughly estimated as the 20%–30% of U_2 from our simulations. We find that w' also depends on λ_b and u_{jet}. As both parameters vary between ISWs, this would suggest a heterogeneous distribution of seed w' and also A_0 over the parameter space. However, we verified that $2u_{jet}/\lambda_b \approx 0.3 - 1.6$ over the parameter space, such that h_b was the dominant factor that determined the order of magnitude of w' in (4.3) and, therefore, of the background noise A_0. A detailed analysis of the effect of seed noise on the BBL instability is beyond the scope of this work. However, we have shown that for roughness elements much smaller than the viscous sublayer thickness, the effect of roughness is equivalent to introducing seed noise to the BBL, which is susceptible to being amplified by the BBL flow.

4.3. *Critical thresholds for instability: experiments versus 2-D spectral simulations*

An immediate consequence of the above analysis is that the definition of general thresholds for instability requires consideration of the background noise level as an additional variable to characterize flow stability. Therefore, to reconcile critical instability thresholds in the laboratory (Carr *et al.* 2008; Zahedi *et al.* 2021) and finite-volume 2-D simulations (Thiem *et al.* 2011; Ellevold & Grue 2023) versus those predicted by 2-D spectral simulations (Diamessis & Redekopp 2006; Aghsaee *et al.* 2012; Posada-Bedoya *et al.* 2024), it is necessary to consider the background noise level, in addition to Re_{ISW} and P_{ISW}.

In the laboratory, the lock-release initialization mechanism of the ISW, bottom roughness, sidewall friction, surface waves, instrument placement, etc., are potential sources of additional noise susceptible to being amplified by the BBL. In flat-bottom 2-D simulations, truncation error and initial and boundary conditions are the main noise sources, depending on the accuracy of the numerical solver.

We estimate that unstable BBLs in the laboratory (Carr *et al.* 2008; Zahedi *et al.* 2021) have a critical $N_c \approx 1.5 - 1.8$ (figure 9b), with an associated background noise $A_0 \approx 10^{-4.8} - 10^{-4.5}$ (figure 12). In comparison, in our flat-bottom spectral 2-D simulations, the unstable BBLs have a critical $N_c \approx 3.3 - 4.0$, with a background noise

$A_0 \approx 10^{-7} - 10^{-6.3}$, which is of the same order as the convergence tolerance of the Generalized Minimum Residual (GMRES) algorithm used for the simulations (10^{-7}). Given that our flat-bottom threshold matches that predicted by the spectral 2-D simulations of Aghsaee *et al.* (2012) (see figure 9*a*), the estimated noise is expected to be of the same order in both solvers. Note that Aghsaee *et al.* (2012) used the spectral solver of Lamb & Nguyen (2009), which was different from ours. This suggests that there is a difference of two orders of magnitude of the background noise between the laboratory experiments versus our 2-D spectral simulations and those by Aghsaee *et al.* (2012), which explains the discrepancy in instability thresholds. This is consistent with the prediction by Verschaeve & Pedersen (2014), who also estimated a difference of two orders of magnitude in the background noise between the laboratory experiments by Carr *et al.* (2008) versus the 2-D spectral simulations by Aghsaee *et al.* (2012). However, their estimated background noise levels assumed $U_\infty \sim \mathcal{O}(1)$, so their actual values for A and A_0 differ from our estimates.

Supported by finite-volume 2-D simulations, Ellevold & Grue (2023) proposed a threshold in terms of a/H, Re_w and d/H, which accurately fit the stability threshold from the laboratory experiments by Carr *et al.* (2008) (see figure 1*b*). They attributed the instability to the truncation error of their numerical solver: 'the growth of the unstable modes arises from the truncation error of the solver at the fifth decimal place'. They defined noise in terms of the vertical velocity fluctuations and quantified it to be $\approx 1 - 2 \times 10^{-5}$ (i.e. $\approx 10^{-5} - 10^{-4.7}$). Interestingly, this is very similar to the background noise level $A_0 \approx 10^{-4.8} - 10^{-4.5}$ estimated herein for laboratory experiments, which is within the threshold region associated with the roughness height $h_b/H = 10^{-5}$ (figure 9*b*). This strongly suggests that the good agreement between the experiments by Carr *et al.* (2008) and the simulations by Ellevold & Grue (2023) is related to the low accuracy of their finite-volume solver, whose background noise amplitude is comparable to that in the laboratory. In comparison, solvers like SPINS and that used by Aghsaee *et al.* (2012) have spectral accuracy. According to our previous analysis, and in agreement with the estimates by Verschaeve & Pedersen (2014), the estimated noise level of spectral solvers is approximately two orders of magnitude smaller than in the laboratory (Carr *et al.* 2008; Zahedi *et al.* 2021) and the simulations by Ellevold & Grue (2023), explaining the discrepancies between the stability thresholds.

The 1 % criterion for spanwise instabilities invoked above was developed for steady homogeneous boundary-layer flow (Croswell 1985; Herbert 1988). Our 2-D simulations cannot resolve these secondary spanwise instabilities. Even in the quasi-steady reference frame moving with the wave, our boundary layer has spatial variations in the locations of the inflection points, which influence the growth of secondary instabilities (Croswell 1985; Herbert 1988). Despite these limitations, we still used the 1 % criterion for when the flow would transition to turbulence. We note that our conclusions from the analysis above would not change by varying the assumed 1 % criterion for triggering secondary spanwise instability. Changes in magnitude to the assumed percentage value would shift all data points equally along the A_0 axis in figure 12(*b*), while the relative magnitude of the background noise would stay the same. Even a 10 % criterion would not change our interpretation of the results.

As noted by Zahedi *et al.* (2021), the combined laboratory data suggest the instability threshold is only determined by $Re_{ISW} \approx 200$, independent of P_{ISW}. Conversely, our analysis indicates that the instability threshold also depends on P_{ISW}. Since the laboratory data only cover a narrow range of $P_{ISW} \approx 0.05 - 0.07$ for $Re_{ISW} \lesssim 200$, it is not possible to use those data to unequivocally establish the independence on P_{ISW}. Therefore, further experiments are required to validate the predicted dependence of the stability threshold on P_{ISW}.

5. Conclusions

We conducted a parametric study on the effects of roughness on BBL instability beneath ISWs of depression. Our simulations show that small-scale bottom roughness changes the stability of the BBL beneath ISWs, for roughness on the same scale as typical flume materials used in a laboratory setting. This indicates that glass and smooth concrete should not be considered "smooth" surfaces in the laboratory setting of an ISW-induced BBL flow. The BBL beneath ISWs behaves as a resonator that preferentially amplifies perturbations with the wavelength of the most unstable mode, analogous to the BBL beneath periodic surface waves and SSWs interacting with bottom roughness.

We interpret BBL–roughness interaction as a mechanism for forcing seed noise in the BBL. Supported by the *N*-factor method for Tollmien–Schlichting waves, we propose relations between the roughness height and the seed noise. By considering the background noise level as an additional variable necessary to characterize the flow stability, our results reconcile the discrepancies between critical thresholds of instability in the laboratory and 2-D finite-volume solvers versus those predicted by 2-D spectral simulations.

Our results motivate future research on the interaction of ISW-induced BBL and deformable sediment beds. Specifically, future research should consider how the interaction of the BBL instability driven by bottom roughness can lead to the formation of morphological structures on deformable beds.

Competing interests. The authors report no conflict of interest.

Appendix A. Grid independence

Figure 13 shows the vorticity fields from ISW 13 over $h_b/H = 10^{-5}$, as simulated using four different grid resolutions. The vorticity is visually identical at all resolutions, hence we can conclude that there is grid independence for $\lambda_b^{OS}/\Delta x > 8$ and $N(z \leq h_b) > 3$. In comparison, all simulations over our parameter space satisfied $\lambda_b^{OS}/\Delta x \geq 15$ and $N(z \leq h_b) \geq 6$.

Appendix B. Orr–Sommerfeld solver

The Orr–Sommerfeld equation represents a generalized eigenvalue problem in matrix form

$$\mathbf{A}\hat{\mathbf{v}} = \omega \mathbf{B}\hat{\mathbf{v}}, \tag{B1}$$

with $\hat{\mathbf{v}}$ as the eigenvector and the complex frequency ω as the eigenvalue. Equation B1 was solved using a Chebyshev collocation method on 250 nodes, following Orszag (1971). Derivatives were computed using Chebyshev differentiation matrices following Weideman & Reddy (2000). The code solves the temporal eigenvalue problem, returning all the sets of modes associated with a given complex wavenumber α, from which we selected ω as the most unstable eigenmode (largest $\Im(\omega)$). The simulated near-bed velocity profile $U(z)$ and the grid used for the stability analysis were extended further away from the wall, so the velocity profile smoothly increased to free-stream conditions.
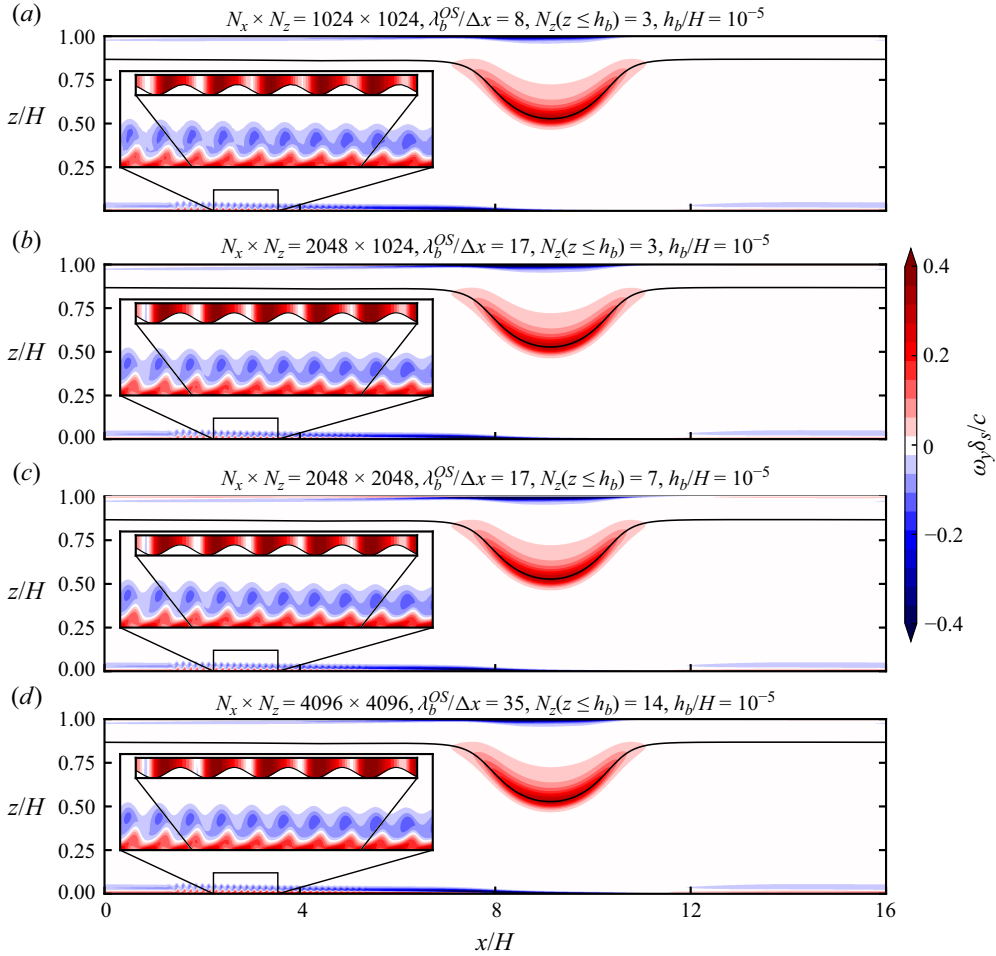
1009 A21-26

Figure 13. Snapshots of the non-dimensional vorticity field ($\omega_y \delta_s / c$) after the passage of ISW 13 over the rough wall region with $h_b/H = 10^{-5}$, as simulated using four different grid resolutions. Each panel shows a near-bed zoom of the vorticity field over the rough wall region and a zoom of the bottom topography.

We validated the code by comparing the most unstable eigenvalue for the Blasius boundary layer with that reported by Gaster (1978). We found agreement with their results over the range $Re_{\delta*}$ 500–3000 to the 6th digit for the real and imaginary parts.

Appendix C. Spacetime instability transformations

Figure 14 shows an example of the 2-D maps and the corresponding spectra of growth and amplification rate computed for a selected velocity profile.

Theoretical transformations between temporal and spatial growth rates can be derived from the dispersion relation of the instability (Gaster 1962; Xu *et al.* 2023). Here, the spatial spectrum estimated from the 2-D analysis was compared with the predicted by Gaster's transformation between temporal (ω_i) and spatial ($-\alpha_i$) spectra (Gaster 1962)
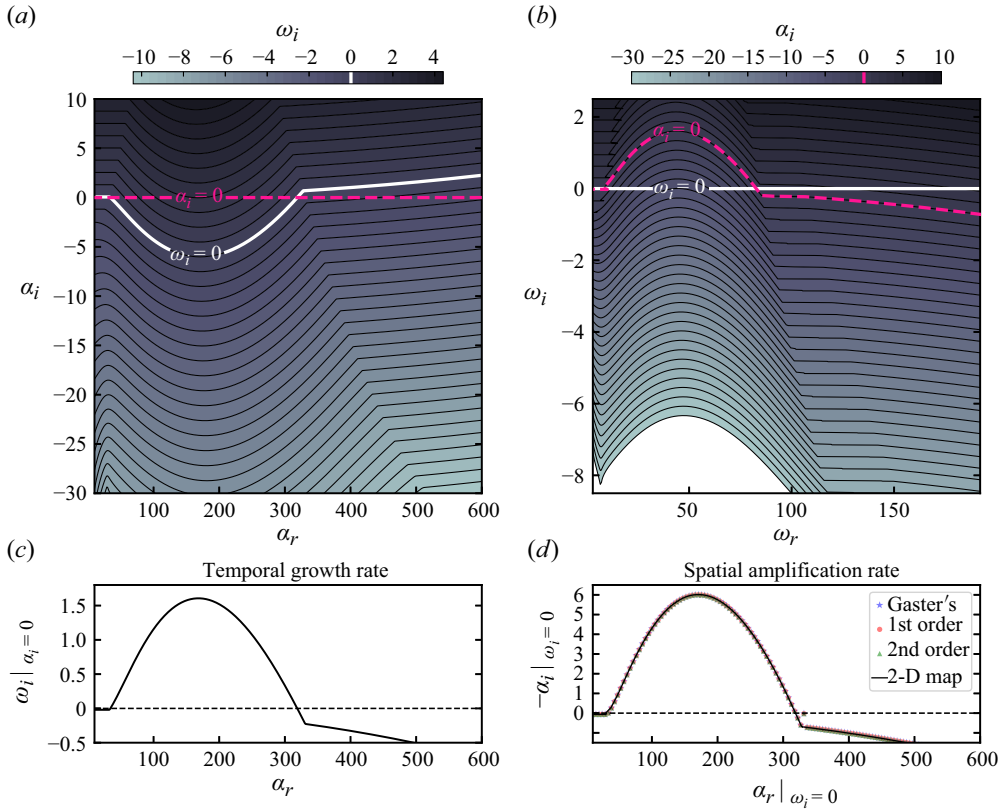
$$-\alpha_i = \frac{\omega_i}{c_g}, \tag{C1}$$

Figure 14. (*a*) Contours of temporal growth rate ω_i on the α_r vs α_i space. (*b*) Contours of spatial amplification rate $-\alpha_i$ on the ω_r vs ω_i space. (*c*) Temporal growth rate spectrum. (*d*) Spatial amplification rate spectrum.

and the first- and second-order transformations proposed by Xu *et al.* (2023)

$$\alpha(S) = \alpha(T) - i\frac{\omega_i(T)}{c_g}, \tag{C2}$$

$$\alpha(S) = \alpha(T) + \frac{\mathrm{d}\omega}{\mathrm{d}\alpha}\left[-1 + \sqrt{1 - 2i\omega_i\frac{\mathrm{d}^2\omega}{\mathrm{d}\alpha^2}/\left(\frac{\mathrm{d}\omega}{\mathrm{d}\alpha}\right)^2}\right]/\frac{\mathrm{d}^2\omega}{\mathrm{d}\alpha^2}, \tag{C3}$$

where $c_g = \partial\omega_r/\partial\alpha_r$ is the real part of the group velocity, which can be calculated in temporal stability analysis. The arguments T and S signify a temporal mode ($\alpha_i(T) = 0$) and spatial mode ($\omega_i(S) = 0$), respectively, with the subscripts r and i denoting the real and imaginary parts of a complex quantity, respectively.

The good agreement between the theoretical transformations and the 2-D map shows that the temporal growth rates are suitable for being transformed into spatial amplification rates using any of these transformations. Of particular interest is that the simplest Gaster transformation provides accurate results.

REFERENCES

AGHSAEE, P. & BOEGMAN, L. 2015 Experimental investigation of sediment resuspension beneath internal solitary waves of depression: solitary wave-induced resuspension. *J. Geophys. Res.: Oceans* **120** (5), 3301–3314.

AGHSAEE, P., BOEGMAN, L., DIAMESSIS, P.J. & LAMB, K.G. 2012 Boundary-layer-separation-driven vortex shedding beneath internal Solitary waves of depression. *J. Fluid Mech.* **690**, 321–344.

AGHSAEE, P., BOEGMAN, L. & LAMB, K.G. 2010 Breaking of shoaling internal solitary waves. *J. Fluid Mech.* **659**, 289–317.

BLONDEAUX, P. & VITTORI, G. 1994 Wall imperfections as a triggering mechanism for Stokes-layer transition. *J. Fluid Mech.* **264**, 107–135.

BOEGMAN, L., IVEY, G.N. & IMBERGER, J. 2005 The degeneration of internal waves in lakes with sloping topography. *Limnol. Oceanogr.* **50** (5), 1620–1637.

BOEGMAN, L. & STASTNA, M. 2019 Sediment resuspension and transport by internal solitary waves. *Annu. Rev. Fluid Mech.* **51** (1), 129–154.

CARR, M. & DAVIES, P.A. 2006 The motion of an internal solitary wave of depression over a fixed bottom boundary in a shallow, two-layer fluid. *Phys. Fluids* **18** (1), 016601.

CARR, M., DAVIES, P.A. & SHIVARAM, P. 2008 Experimental evidence of internal solitary wave-induced global instability in shallow water benthic boundary layers. *Phys. Fluids* **20** (6), 066603.

CARR, M., STASTNA, M. & DAVIES, P.A. 2010 Internal solitary wave-induced flow over a corrugated bed. *Ocean Dyn.* **60** (4), 1007–1025.

CHANG, M.-H., LIEN, R.-C., TANG, T.Y., D'ASARO, E.A. & YANG, Y.J. 2006 Energy flux of nonlinear internal waves in northern south china sea. *Geophys. Res. Lett.* **33**, L03607.

CROSWELL, J.W. 1985 On the energetics of primary and secondary instabilities in plane poiseuille flow *PhD thesis*, Virginia Polytechnic Institute and State University.

DARBY, R. & CHHABRA, R.P. 2017 *Chemical Engineering Fluid Mechanics*. Third edn. CRC Press.

DEEPWELL, D., CLARRY, C., SUBICH, C. & STASTNA, M. 2021 Vortex generation due to internal solitary wave propagation past a sidewall constriction. *J. Fluid Mech.* **913**, A47–26.

DIAMESSIS, P.J. & REDEKOPP, L.G. 2006 Numerical investigation of solitary internal wave-induced global instability in shallow water benthic boundary layers. *J. Phys. Oceanogr.* **36** (5), 784–812.

DIWAN, S.S. & RAMESH, O.N. 2012 Relevance of local parallel theory to the linear stability of laminar separation bubbles. *J. Fluid Mech.* **698**, 468–478.

DRAZIN, P.G. & REID, W.H. 1981 *Hydrodynamic Stability*. 2nd edn edn. Cambridge University Press.

DUNPHY, M., SUBICH, C. & STASTNA, M. 2011 Spectral methods for internal waves: indistinguishable density profiles and double-humped solitary waves. *Nonlinear Process. Geophys.* **18** (3), 351–358.

ELLEVOLD, T.J. & GRUE, J. 2023 Calculation of internal-wave-driven instability and vortex shedding along a flat bottom. *J. Fluid Mech.* **966**, A40.

GASTER, M. 1962 A note on the relation between temporally-increasing and spatially-increasing disturbances in hydrodynamic stability. *J. Fluid Mech.* **14** (2), 222–224.

GASTER, M. 1978 Series representation of the eigenvalues of the Orr-Sommerfeld equation. *J. Comput. Phys.* **29** (2), 147–162.

GHASSEMI, A., ZAHEDI, S. & BOEGMAN, L. 2022 Bolus formation from fission of nonlinear internal waves over a mild slope. *J. Fluid Mech.* **932**, A50.

HARNANAN, S., SOONTIENS, N. & STASTNA, M. 2015 Internal wave boundary layer interaction: a novel instability over broad topography. *Phys. Fluids* **27** (1), 016605.

HARNANAN, S., STASTNA, M. & SOONTIENS, N. 2017 The effects of near-bottom stratification on internal wave induced instabilities in the boundary layer. *Phys. Fluids* **29** (1), 016602.

HARTHARN-EVANS, S.G., CARR, M., STASTNA, M. & DAVIES, P.A. 2022 Stratification effects on shoaling internal solitary waves. *J. Fluid Mech.* **933**, A19.

HERBERT, T. 1988 Secondary instability of boundary layers. *Annu. Rev. Fluid Mech.* **20** (1), 487–526.

HERBERT, T. 1997 Parabolized stability equations. *Annu. Rev. Fluid Mech.* **29** (1), 245–283.

HUERRE, P. & MONKEWITZ, P.A. 1990 Local and global instabilities in spatially developing flows. *Annu. Rev. Fluid Mech.* **22** (1), 473–537.

JONES, L.E., SANDBERG, R.D. & SANDHAM, N.D. 2008 Direct numerical simulations of forced and unforced separation bubbles on an airfoil at incidence. *J. Fluid Mech.* **602**, 175–207.

KLYMAK, J.M. & MOUM, J.N. 2003 Internal solitary waves of elevation advancing on a shoaling shelf. *Geophys. Res. Lett.* **30**, 2045.

KUPFER, K., BERS, A. & RAM, A.K. 1987 The cusp map in the complex-frequency plane for absolute instabilities. *Phys. Fluids* **30** (10), 3075–3082.

LAMB, K.G. & NGUYEN, V.T. 2009 Calculating energy flux in internal solitary waves with an application to reflectance. *J. Phys. Oceanogr.* **39** (3), 559–580.

MARXEN, O., LANG, M., RIST, U. & WAGNER, S. 2003 A combined experimental/numerical study of unsteady phenomena in a laminar separation bubble. *Flow Turbul. Combust.* **71** (1-4), 133–146.

MICHALLET, H. & IVEY, G.N. 1999 Experiments on mixing due to internal solitary waves breaking on uniform slopes. *J. Geophys. Res.: Oceans* **104** (C6), 13467–13477.

MOUM, J.N., FARMER, D.N., SHROYER, E.L., SMYTH, W.D. & ARMI, L. 2007*a* Dissipative losses in nonlinear internal waves propagating across the continental shelf. *J. Phys. Oceanogr.* **37** (7), 1989–1995.

MOUM, J.N., KLYMAK, J.M., NASH, J.D., PERLIN, A. & SMYTH, W.D. 2007*b* Energy transport by nonlinear internal waves. *J. Phys. Oceanogr.* **37** (7), 1968–1988.

OLSTHOORN, J. & STASTNA, M. 2014 Numerical investigation of internal wave-induced sediment motion: resuspension versus entrainment. *Geophys. Res. Lett.* **41** (8), 2876–2882.

ORSZAG, S.A. 1971 Accurate solution of the orr–sommerfeld stability equation. *J. Fluid Mech.* **50** (4), 689–703.

OZDEMIR, C.E., HSU, T.-J. & BALACHANDAR, S. 2013 Direct numerical simulations of instability and boundary layer turbulence under a solitary wave. *J. Fluid Mech.* **731**, 545–578.

POSADA-BEDOYA, A., OLSTHOORN, J. & BOEGMAN, L. 2024 The boundary layer instability beneath internal solitary waves and its sensitivity to vortex wakes. *J. Fluid Mech.* **990**, A18.

SAKAI, T., DIAMESSIS, P.J. & JACOBS, G.B. 2020 Self-sustained instability, transition, and turbulence induced by a long separation bubble in the footprint of an internal solitary wave I. Flow Topology. *Phys. Rev. Fluids* **5** (10), 103801.

SCANDURA, P. 2013 Two-dimensional vortex structures in the bottom boundary layer of progressive and solitary waves. *J. Fluid Mech.* **728**, 340–361.

SCHLICHTING, H. 1968 *Boundary Layer Theory*. 6th edn edn. McGraw-Hill.

SCHMID, P.J. & HENNINGSON, D.S. 2001 Stability and transition in shear flows. In *Applied Mathematical Sciences*, vol. **142**. Springer New York.

SHROYER, E.L., MOUM, J.N. & NASH, J.D. 2009 Observations of polarity reversal in shoaling nonlinear internal waves. *J. Phys. Oceanogr.* **39** (3), 691–701.

SHROYER, E.L., MOUM, J.N. & NASH, J.D. 2010 Energy transformations and dissipation of nonlinear internal waves over new jersey's continental shelf. *Nonlinear Process. Geophys.* **17** (4), 345–360.

STASTNA, M. & LAMB, K.G. 2008 Sediment resuspension mechanisms associated with internal waves in coastal waters. *J. Geophys. Res.: Oceans* **113** (C10), C10016.

SUBICH, C.J., LAMB, K.G. & STASTNA, M. 2013 Simulation of the Navier–Stokes equations in three dimensions with a spectral collocation method. *Intl J. Numer. Meth. Fluids* **73** (2), 103–129.

SUMER, B.M., JENSEN, P.M., SØRENSEN, L.B., FREDSØE, J., LIU, P.L.-F. & CARSTENSEN, S. 2010 Coherent structures in wave boundary layers. part 2. solitary motion. *J. Fluid Mech.* **646**, 207–231.

THIEM, Ø, CARR, M., BERNTSEN, J. & DAVIES, P.A. 2011 Numerical simulation of internal solitary wave–induced reverse flow and associated vortices in a shallow, two-layer fluid benthic boundary layer. *Ocean Dyn.* **61** (6), 857–872.

TROWBRIDGE, J.H. & LENTZ, S.J. 2018 The bottom boundary layer. *Annu. Rev. Mar. Sci.* **10** (1), 397–420.

TURKINGTON, B., EYDELAND, A. & WANG, S. 1991 A computational method for solitary internal waves in a continuously stratified fluid. *Stud. Appl. Maths* **85** (2), 93–127.

VERSCHAEVE, J.C.G. & PEDERSEN, G.K. 2014 Linear stability of boundary layers under solitary waves. *J. Fluid Mech.* **761**, 62–104.

VITTORI, G. & BLONDEAUX, P. 2011 Characteristics of the boundary layer at the bottom of a solitary wave. *Coast. Engng* **58** (2), 206–213.

WEIDEMAN, J.A. & REDDY, S.C. 2000 A matlab differentiation matrix suite. *ACM Trans. Math. Softw. (TOMS)* **26** (4), 465–519.

XU, J., LIU, J., ZHANG, Z. & WU, X. 2023 Spatial–temporal transformation for primary and secondary instabilities in weakly non-parallel shear flows. *J. Fluid Mech.* **959**, A21.

ZAHEDI, S., AGHSAEE, P. & BOEGMAN, L. 2021 Internal solitary wave bottom boundary layer dissipation. *Phys. Rev. Fluids* **6** (7), 074802.

ZAHEDI, S., GHASSEMI, A. & BOEGMAN, L. 2023 Bolus degeneration on uniform slopes. *Estuar. Coast. Shelf Sci.* **280**, 108190.

ZULBERTI, A., JONES, N.L. & IVEY, G.N. 2020 Observations of enhanced sediment transport by nonlinear internal waves. *Geophys. Res. Lett.* **47** (19), e2020GL088499.

ZULBERTI, A.P., JONES, N.L., RAYSON, M.D. & IVEY, G.N. 2022 Mean and turbulent characteristics of a bottom mixing-layer forced by a strong surface tide and large amplitude internal waves. *J. Geophys. Res.: Oceans* **127** (1), e2020JC017055.